

REPELLING-ATTRACTING HAMILTONIAN MONTE CARLO

SIDDHARTH VISHWANATH^{*1} AND HYUNGSUK TAK^{2,3,4}

¹DEPARTMENT OF MATHEMATICS, UNIVERSITY OF CALIFORNIA, SAN DIEGO

²DEPARTMENT OF STATISTICS, PENNSYLVANIA STATE UNIVERSITY

³DEPARTMENT OF ASTRONOMY AND ASTROPHYSICS, PENNSYLVANIA STATE UNIVERSITY

⁴INSTITUTE FOR COMPUTATIONAL AND DATA SCIENCES, PENNSYLVANIA STATE UNIVERSITY

Abstract

We propose a variant of Hamiltonian Monte Carlo (HMC), called the Repelling-Attracting Hamiltonian Monte Carlo (RAHMC), for sampling from multimodal distributions. The key idea that underpins RAHMC is a departure from the conservative dynamics of Hamiltonian systems, which form the basis of traditional HMC, and turning instead to the dissipative dynamics of conformal Hamiltonian systems. In particular, RAHMC involves two stages: a mode-repelling stage to encourage the sampler to move away from regions of high probability density; and, a mode-attracting stage, which facilitates the sampler to find and settle near alternative modes. We achieve this by introducing just one additional tuning parameter—the coefficient of friction. The proposed method adapts to the geometry of the target distribution, e.g., modes and density ridges, and can generate proposals that cross low-probability barriers with little to no computational overhead in comparison to traditional HMC. Notably, RAHMC requires no additional information about the target distribution or memory of previously visited modes. We establish the theoretical basis for RAHMC, and we discuss repelling-attracting extensions to several variants of HMC in literature. Finally, we provide a tuning-free implementation via dual-averaging, and we demonstrate its effectiveness in sampling from, both, multimodal and unimodal distributions in high dimensions.

1 Introduction

Consider the problem of drawing samples $\{\mathbf{q}_1, \mathbf{q}_2, \mathbf{q}_3, \dots\} \subset \mathbb{R}^d$ from a target distribution, π , whose probability density function is given by

$$\pi(\mathbf{q}) = \frac{1}{Z} \exp(-U(\mathbf{q})),$$

where $\mathbf{q} = (q_1, q_2, \dots, q_d) \in \mathbb{R}^d$, $U(\mathbf{q}) := -\log \pi(\mathbf{q})$, and $Z = \int \exp(-U(\mathbf{q})) d\mathbf{q}$ is its normalizing constant. Such problems are prevalent in Bayesian inference (Gelman et al., 1995), probabilistic machine learning (Andrieu et al., 2003), and statistical physics (Binder et al., 1992), among other fields, and constitutes the core of Markov chain Monte Carlo (MCMC) methods. The goal of MCMC is to generate a sequence of dependent samples $\{\mathbf{q}_1, \mathbf{q}_2, \dots, \mathbf{q}_n\}$ that converges to the target distribution π as $n \rightarrow \infty$ (Brooks et al., 2011).

In most practical settings, the analytical expression for the normalizing constant Z is seldom available, or, its numerical computation is intractable. Therefore, sampling from the target distribution $\pi(\mathbf{q})$ can become an insurmountable task (Møller et al., 2006, Murray et al., 2012, Park and Haran, 2018). The Metropolis-Hastings

*Corresponding author: svishwanath@ucsd.edu

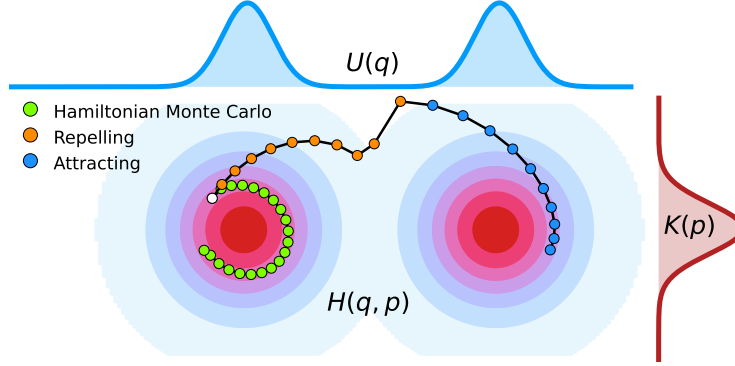


Figure 1: Illustration of rAHMC and HMC transitions for a bimodal target distribution $\pi(\mathbf{q}) = -\log(U(\mathbf{q}))$ in an extended phase space; $U(\mathbf{q})$ is the potential energy, $K(\mathbf{p})$ is the kinetic energy, and $H(\mathbf{q}, \mathbf{p}) = U(\mathbf{q}) + K(\mathbf{p})$ is the Hamiltonian. The rAHMC trajectory concatenates two conformal Hamiltonian trajectories to generate the final proposal. The first trajectory (in orange) simulates the mode-repelling dynamics, forcing the trajectory to move away from the current mode. The second trajectory (in blue) simulates the mode-attracting dynamics, and the trajectory is drawn towards a different mode. Combined, the rAHMC trajectory is able to jump between modes by moving *across* the energy level sets of $H(\mathbf{q}, \mathbf{p})$. This is in contrast to HMC, which moves *along* the energy level sets of $H(\mathbf{q}, \mathbf{p})$, and is unable to jump between modes.

algorithm (Metropolis et al., 1953, Hastings, 1970), overcomes this by generating proposals from a random walk. However, the random walk nature of the Metropolis-Hastings algorithm makes it inefficient for sampling from high-dimensional target distributions.

Hamiltonian Monte Carlo (HMC; Duane et al., 1987, Neal, 2011) along with its tuning-free implementations, such as the No-U-Turn sampler (NUTS; Hoffman and Gelman, 2014), have emerged as the mainstay for sampling from high dimensional distributions when the gradient information, $\nabla \log \pi(\mathbf{q})$, is available. HMC broadly falls under the category of MCMC methods based on data augmentation (Tanner and Wong, 1987, van Dyk and Meng, 2001), whereby an auxiliary variable $\mathbf{p} = (p_1, p_2, \dots, p_d) \in \mathbb{R}^d$, specified by its density function $\pi(\mathbf{p}) \propto \exp(-K(\mathbf{p}))$, is introduced such that the joint distribution of (\mathbf{q}, \mathbf{p}) is given by

$$\pi(\mathbf{q}, \mathbf{p}) \propto \exp(-U(\mathbf{q}) - K(\mathbf{p})) =: \exp(-H(\mathbf{q}, \mathbf{p})).$$

By regarding \mathbf{q} as its position of a particle with potential energy $U(\mathbf{q})$, and \mathbf{p} as its conjugate momentum with kinetic energy $K(\mathbf{p})$, the term $H(\mathbf{q}, \mathbf{p})$ can be interpreted as the Hamiltonian of a physical system in an extended phase space $(\mathbf{q}, \mathbf{p}) \in \mathbb{R}^{2d}$. Given the current state \mathbf{q} , the key idea of HMC is to sample $\mathbf{p} \sim \pi(\mathbf{p})$ from a known distribution and generate a proposal $(\mathbf{q}, \mathbf{p}) \mapsto (\mathbf{q}_T, \mathbf{p}_T)$ by simulating the Hamiltonian dynamics of the system for a fixed time T , i.e.,

$$\frac{d}{dt} \mathbf{q}_t = \nabla_{\mathbf{p}} H(\mathbf{p}_t, \mathbf{p}_t) = \nabla K(\mathbf{p}_t), \quad \text{and} \quad \frac{d}{dt} \mathbf{p}_t = -\nabla_{\mathbf{q}} H(\mathbf{q}, \mathbf{p}) = \nabla U(\mathbf{q}).$$

The green trajectory in Figure 1 illustrates a typical HMC proposal. Unlike the random-walk Metropolis method, by leveraging information from $\nabla U(\mathbf{q}) = -\nabla \log \pi(\mathbf{q})$, HMC is able to adapt to the geometry of the target distribution, and produce distant proposals with high acceptance probabilities even in high dimensions. We refer the reader to Neal (2011) and Betancourt (2017) for a detailed review of HMC.

Several lines of work have extended the HMC algorithm to situations where the $\log \pi(\mathbf{q})$ is discontinuous (Nishimura et al., 2020), when the support of π is discrete (Zhang et al., 2012), when the support of π is a Riemannian manifold (Girolami and Calderhead, 2011), or when the gradient evaluation is intractable (Strathmann et al., 2015). However, a fundamental shortcoming of HMC is its inability to sample from multimodal distributions, and is widely acknowledged in literature (e.g., Barp et al., 2018). In particular,

since $\nabla U(\mathbf{q})$ only captures local information, HMC is unable to traverse and generate proposals across well-separated regions of π . This is particularly problematic in high-dimensional settings, where zero-density regions are more prevalent, and the modes of π are more likely to be well-separated.

In order to address the shortcomings of HMC for multimodal target distributions, several methods have been proposed in the literature. Broadly, they may be classified into the following three categories: (i) methods that generalize the original HMC dynamics to that of another physical system (e.g., Leimkuhler and Reich, 2009, Tripuraneni et al., 2017, Liu and Zhang, 2019), (ii) methods which lower the energy barrier between modes by augmenting the phase-space via auxiliary variables, or via tempering schemes (e.g., Betancourt, 2014, Nishimura and Dunson, 2016, Graham and Storkey, 2017, Nemeth et al., 2019, Park, 2021, Alenlöv et al., 2021), and (iii) methods that introduce a systematic method for identifying where the modes of the distribution are, and then adapting the HMC dynamics to jump between these modes (e.g., Sminchisescu and Welling, 2011, Lan et al., 2014, Pompe et al., 2020). Section 2.3 provides a more detailed review of these methods. Implementing these methods often requires additional tuning parameters, and are computationally more expensive than traditional HMC.

In this paper we propose the Repelling-Attracting Hamiltonian Monte Carlo (RAHMC) algorithm for sampling from both unimodal and multimodal distributions. The philosophy underlying RAHMC is to generate proposals in two stages: in the first stage, high-density regions of π act as repelling states and encourage the trajectory to move away from them into low density regions, and, in the second state, the high-density regions act as attracting states and encourage the trajectory to settle near them. The orange and blue trajectories in Figure 1 illustrate a typical RAHMC proposal. This is achieved by moving away from the physical interpretation of Hamiltonian dynamics and by considering, instead, conformal Hamiltonian systems where energy can be created and dissipated. Therefore, our method can be described as a middle-ground between the perspectives, (ii) and (iii), described above. Our main contributions are the following:

- We propose a new MCMC sampler, RAHMC, that is designed to be a versatile sampler for both unimodal and multimodal distributions, which requires only one additional tuning parameter, γ , the coefficient of friction, in addition to the default tuning parameters of HMC.
- We show that RAHMC satisfies the key properties which make HMC a successful MCMC sampler, and demonstrate that RAHMC can maintain high acceptance rate across long trajectories across multiple modes even in high dimensions.
- We provide an automatic tuning procedure of RAHMC using dual-averaging method of Nesterov (2009), akin to the automatic tuning procedure for the No-U-Turn sampler and HMC (Hoffman and Gelman, 2014).
- We show that RAHMC can be generalized to incorporate other variants of HMC, e.g., relativistic Monte-Carlo (Lu et al., 2017), magnetic HMC (Tripuraneni et al., 2017), and the non-canonical HMC (Brofos and Lederman, 2020), among others.

The code for the implementation and for reproducing the experiments is made publicly available at <https://github.com/sidv23/ra-hmc>.

Notations. For a space X , the map $\text{id} : X \rightarrow X$ is the identity map given by $\text{id}(x) = x$ for all $x \in X$. We use $\mathbf{1}_d, \mathbf{0}_d \in \mathbb{R}^d$ to denote the vector of ones and zeros in \mathbb{R}^d , \mathbf{I}_d to denote the $d \times d$ identity matrix, and \mathbf{O}_d to denote the $d \times d$ zero matrix. We drop the subscript d when the dimensionality is clear from the context. For a vector $\mathbf{x} \in \mathbb{R}^{2k}$, we use $\text{proj}_1(\mathbf{x})$ and $\text{proj}_2(\mathbf{x})$ to be the projection of \mathbf{x} onto the first and last k components, respectively. $\mathcal{N}(\mu, \Sigma)$ denotes the multivariate Gaussian distribution with mean $\mu \in \mathbb{R}^d$

and covariance matrix $\Sigma \in \mathbb{R}^{d \times d}$. For a differentiable function $f : \mathbb{R}^d \rightarrow \mathbb{R}$ the gradient and Hessian of f are denoted by ∇f and $\nabla^2 f$, respectively, and for $F : \mathbb{R}^d \rightarrow \mathbb{R}^p$, $\mathbf{D}F$ is the $d \times p$ Jacobian matrix.

As per convention in MCMC literature, and with a slight overload of notation, we use π as a general notation to represent the target distribution that we aim to sample from, and $\text{supp}(\pi)$ to denote its support. The exact distribution will be made precise in context. Throughout this work, we assume that $-\log \pi(\mathbf{q})$ is continuously differentiable and ℓ -Lipschitz for some $\ell > 0$.

2 Background

In this section, we provide the necessary background on Hamiltonian Monte Carlo (HMC), which forms the basis of our proposed method. We begin by detailing the general methodology of HMC in Section 2.1, and summarize the key characteristics that contribute to the success of HMC in Section 2.2. Finally, in Section 2.3, we explore the primary challenges when sampling from multimodal distributions and examine the existing literature that tackles this issue. We refer the reader to Neal (2011), Betancourt (2017) and Betancourt et al. (2017) for a comprehensive overview of HMC and its theoretical underpinnings.

2.1 Hamiltonian Monte Carlo

Let $\pi(\mathbf{q})$ be a target distribution whose probability density function is given by $\pi(\mathbf{q}) \propto \exp(-U(\mathbf{q}))$, where $\mathbf{q} = (q_1, q_2, \dots, q_d) \in \mathbb{R}^d$. By augmenting the target distribution with an auxiliary momentum variable $\mathbf{p} = (p_1, p_2, \dots, p_d) \in \mathbb{R}^d$, whose marginal distribution is given by $\pi(\mathbf{p}) \propto \exp(-K(\mathbf{p}))$ for a user-specified choice of $K(\mathbf{p})$, the joint target distribution of (\mathbf{q}, \mathbf{p}) is given by

$$\pi(\mathbf{q}, \mathbf{p}) \propto \exp(-U(\mathbf{q}) - K(\mathbf{p})) =: \exp(-H(\mathbf{q}, \mathbf{p})).$$

With an appropriate distribution for \mathbf{p} , the resulting energy function $H(\mathbf{q}, \mathbf{p}) := U(\mathbf{q}) + K(\mathbf{p})$ can be characterized as the Hamiltonian for the system in an *extended phase space* $(\mathbf{q}, \mathbf{p}) \in \mathbb{R}^{2d}$, where \mathbf{q} corresponds to the position of a particle, and \mathbf{p} corresponds to its (conjugate) momentum. The functions $U(\mathbf{q}) := -\log \pi(\mathbf{q})$ and $K(\mathbf{p})$ are commonly referred to as the potential energy function and the kinetic energy functions, respectively.

Hamiltonian Monte Carlo (HMC) generates samples from $\pi(\mathbf{q})$ by first resampling auxiliary momentum $\mathbf{p} \sim \pi(\mathbf{p})$, and then simulating Hamiltonian dynamics in the extended phase space $(\mathbf{q}, \mathbf{p}) \in \mathbb{R}^{2d}$ for a time interval T . The auxiliary momentum \mathbf{p} is subsequently discarded to obtain samples from the target distribution $\pi(\mathbf{q})$. The HMC algorithm proceeds as follows: given the initial Markov chain state $(\mathbf{q}_0, \mathbf{p}_0)$, the particle is subject to the dynamics given by

$$\frac{d}{dt} \begin{pmatrix} \mathbf{q}_t \\ \mathbf{p}_t \end{pmatrix} = \underbrace{\begin{bmatrix} \mathbf{O} & \mathbf{I} \\ -\mathbf{I} & \mathbf{O} \end{bmatrix}}_{=: \Omega} \begin{pmatrix} \nabla U(\mathbf{q}_t) \\ \nabla K(\mathbf{p}_t) \end{pmatrix}. \quad (1)$$

By taking $\mathbf{z}_t = (\mathbf{q}_t, \mathbf{p}_t)$, Eq. (1) can be concisely written as the Hamiltonian flow

$$\frac{d}{dt} \mathbf{z}_t = \Omega \nabla_{\mathbf{z}} H(\mathbf{z}_t), \quad (2)$$

where the skew-symmetric matrix Ω can be thought of as the coordinate representation for the symplectic structure underlying the Hamiltonian system. The position of the particle at time t is given by the integral operator $\Phi_t : \mathbb{R}^{2d} \rightarrow \mathbb{R}^{2d}$, where $\mathbf{z}_t = \Phi_t(\mathbf{z}_0)$ is obtained by solving the autonomous system of differential equations in Eq. (2). Then, the proposed state at time T is obtained by applying a momentum-flip operation

to z_T , that is, $\tilde{z}_T = \mathbf{F}(z_T)$ where $\mathbf{F} : (\mathbf{q}, \mathbf{p}) \mapsto (\mathbf{q}, -\mathbf{p})$. Finally, the proposed state \tilde{z}_T is accepted/rejected via a Metropolis-Hastings acceptance probability given the current state z ,

$$\alpha(\tilde{z}_T | z) := \min \left\{ 1, \exp \left(-H(\tilde{z}_T) + H(z) \right) \times \left| \det \left(\frac{d\tilde{z}_T}{dz} \right) \right| \right\}. \quad (3)$$

Remark 2.1. *The HMC methodology offers flexibility in the choice of the distribution for the auxiliary momentum \mathbf{p} , $\pi(\mathbf{p}) \propto \exp(-K(\mathbf{p}))$. However, in practice, $K(\mathbf{p})$ is typically taken to be*

$$K(\mathbf{p}) = \frac{1}{2} \mathbf{p}^\top \boldsymbol{\Sigma}^{-1} \mathbf{p},$$

such that the momentum variable is sampled from a Gaussian distribution, i.e., $\mathbf{p} \sim \mathcal{N}(\mathbf{0}, \boldsymbol{\Sigma})$.

While the flow operator Φ_T , corresponding to the Hamiltonian flow in Eq. (2), is seldom available analytically, efficient numerical integrators based on splitting methods are widely available, such as the Störmer-Verlet/leapfrog scheme (Hairer et al., 2006). In the leapfrog scheme, the Hamiltonian of the system is split into three parts, i.e.,

$$H(z) = H_1(z) + H_2(z) + H_3(z) = \frac{1}{2}U(\mathbf{q}) + K(\mathbf{p}) + \frac{1}{2}K(\mathbf{q}).$$

Then, for a step-size $\epsilon \approx dt$ and $i = 1, 2, 3$, the flow Φ_{dt} associated with each sub-Hamiltonian H_i in time interval $(t, t + \epsilon]$ is numerically approximated by maps $\xi_{\epsilon, i}$. The resulting flow is given by $\Phi_\epsilon := \xi_1 \circ \xi_2 \circ \xi_3 \approx \Phi_{dt}$, where

$$\xi_1(\mathbf{q}, \mathbf{p}) = \xi_3(\mathbf{q}, \mathbf{p}) = \left(\mathbf{q}, \mathbf{p} - \frac{\epsilon}{2} \nabla U(\mathbf{q}) \right) \quad \text{and} \quad \xi_2(\mathbf{q}, \mathbf{p}) = \left(\mathbf{q} + \epsilon \boldsymbol{\Sigma}^{-1} \mathbf{p}, \mathbf{p} \right). \quad (4)$$

Thus, the position of a particle at time T , z_T , is numerically approximated by applying Φ_ϵ consecutively $L = \lfloor T/\epsilon \rfloor$ times, i.e.,

$$z_T = \Phi_{\epsilon, L}(z) := (\Phi_\epsilon)^L(z) = \Phi_\epsilon \circ \Phi_\epsilon \circ \dots \circ \Phi_\epsilon(z).$$

2.2 Key Properties of Hamiltonian Monte Carlo

The success of HMC as a sampling method crucially hinges on the following properties.

℘1. Reversibility. Given the current state z , the proposed states, $z \mapsto \Phi_T(z)$ and $z \mapsto \Phi_{\epsilon, L}(z)$, in HMC constitute a deterministic Markov kernel. From Tierney (1994), a deterministic Markov kernel $\kappa : \mathbb{R}^{2d} \rightarrow \mathbb{R}^{2d}$ satisfies detailed-balance if and only if κ is an involution, i.e., $\kappa \circ \kappa = \text{id}$. Although Φ_T and $\Phi_{\epsilon, L}$, by themselves, are not involutions; when they are composed with the momentum-flip operator, \mathbf{F} , the resulting transition kernels, $\mathbf{F} \circ \Phi_t$ and $\mathbf{F} \circ \Phi_{\epsilon, L}$, are involutions, i.e., $(\mathbf{F} \circ \Phi_t) \circ (\mathbf{F} \circ \Phi_t) = \text{id}$, and $(\mathbf{F} \circ \Phi_{\epsilon, L}) \circ (\mathbf{F} \circ \Phi_{\epsilon, L}) = \text{id}$. Therefore, the momentum flip operation in Eq. (3) is crucial for ensuring that the resulting Markov chain satisfies the detailed-balance condition.

℘2. Volume Preservation. Liouville's theorem (Arnold, 2013, Chapter 3.16 B) guarantees that the Hamiltonian flow, Φ_t , preserves volume in the phase space, i.e., $|\det(\mathbf{D}\Phi_t(z))| = 1$ for all $t \in \mathbb{R}$. Since the momentum flip operator \mathbf{F} is also volume-preserving, the Jacobian term appearing in Eq. (3) becomes

$$\det \left(\frac{d\tilde{z}_T}{dz} \right) = \det(\mathbf{D}(\mathbf{F} \circ \Phi_T)(z)) = \det(\mathbf{F}) \times \det(\mathbf{D}\Phi_T(z)) = 1,$$

where the second equality follows from the Jacobian chain rule. This ensures that the Jacobi determinant appearing in Eq. (3) is always 1, and substantially reduces the computational cost of computing α in Eq. (3). See, for example, Levy et al. (2018), where sacrificing volume preservation warrants careful adjustments in order to make the resulting algorithm computationally tractable.

$\mathcal{P}3$. Energy conservation. Hamiltonian dynamics traverses iso-energy contours in the extended phase space, and the flow Φ_t preserves the Hamiltonian, i.e.,

$$\frac{d}{dt}H(\mathbf{z}_t) = 0.$$

Thus, $H(\Phi_t(\mathbf{z})) = H(\mathbf{z})$ for all $t \in [0, T]$. Combined with the fact that the momentum-flip operator preserves the Hamiltonian, i.e., $H(\mathbf{F}(\mathbf{z})) = H(\mathbf{z})$, it follows that $H(\tilde{\mathbf{z}}_T) = H(\mathbf{F} \circ \Phi_T(\mathbf{z})) = H(\mathbf{z})$, and the energy in the proposed state $\tilde{\mathbf{z}}_T$ is also preserved. Therefore, in combination with ($\mathcal{P}2$), if the Hamiltonian dynamics can be exactly simulated, then the resulting proposal $\tilde{\mathbf{z}}_T$ can be accepted with probability 1.

$\mathcal{P}4$. Symplecticity. Hamiltonian systems encode strong symmetries, which are made precise using machinery from differential geometry; see Betancourt et al. (2017) for an overview. In particular, the *symplectic* 2-form, ω , encapsulates the conservation laws and dynamical evolution prescribed by Hamiltonian dynamics. Informally, the symplectic 2-form, denoted by the wedge product

$$\omega = d\mathbf{q} \wedge d\mathbf{p} = \sum_{i=1}^d dq_i \wedge dp_i,$$

measures the oriented area spanned by infinitesimal displacements in position, \mathbf{q} , and the momentum, \mathbf{p} . Remarkably, in addition to the volume preservation in ($\mathcal{P}2$), the Hamiltonian flow Φ_t preserves symplectic form ω , or, equivalently, from Arnold (2013, Chapter 9.44 D),

$$\left(\frac{d\mathbf{z}_t}{d\mathbf{z}}\right)^\top \Omega^{-1} \left(\frac{d\mathbf{z}_t}{d\mathbf{z}}\right) = \mathbf{D}\Phi_t(\mathbf{z})^\top \Omega^{-1} \mathbf{D}\Phi_t(\mathbf{z}) = \Omega^{-1} \quad \text{for all } t \in \mathbb{R}.$$

Therefore, it follows that preserving symplectic structure also guarantees that volume is conserved.

Notably, however, preserving symplectic structure provides access to *symplectic integrators*, $\Phi_{\epsilon,L}$, to approximate the continuous-time flow Φ_T . Like their continuous time analogues, symplectic integrators also preserve the symplectic form (and, therefore, volume) in phase space, and satisfy reversibility à-la ($\mathcal{P}1$) (Hairer et al., 2006). Some notable examples include (first-order) symplectic Euler integrator, the (second-order) leapfrog integrators and (higher-order) Yoshida integrators.

Moreover, even though symplectic integrators do not preserve the Hamiltonian $H(\mathbf{z})$, they exactly preserve a *shadow Hamiltonian* (Hairer et al., 2006, Chapter IX, Theorem 3.2) whose approximation error is strongly controlled for the integration time T . For instance, for the leapfrog integrator the global error is

$$\|\Phi_T(\mathbf{z}) - \Phi_{\epsilon,L}(\mathbf{z})\| = O(\epsilon^2) \quad \text{for } T = \epsilon L.$$

Moreover, it can be shown (see, e.g., Hairer et al., 2006, Chapter IX, Section 8) that there exists a constant $C > 0$ such that for exponentially long simulation lengths, $T = O(\epsilon^2 e^{C/\epsilon})$, the energy drift is controlled by $|H(\Phi_T(\mathbf{z})) - H(\Phi_{\epsilon,L}(\mathbf{z}))| = O(\epsilon^2)$. Consequently, the acceptance ratio for the proposed state $\tilde{\mathbf{z}}_T = \mathbf{F} \circ \Phi_{\epsilon,L}(\mathbf{z})$ in Eq. (3) is

$$\alpha(\mathbf{F} \circ \Phi_{\epsilon,L}(\mathbf{z}) \mid \mathbf{z}) = \exp(-O(\epsilon^2)),$$

which ensures that the acceptance probability remains relatively high, even for fairly distant trajectories.

2.3 Drawbacks of Hamiltonian Monte Carlo for Multimodal Target Distributions

The inability of HMC to sample effectively from multimodal distribution has been widely acknowledged in literature (e.g., Celeux et al., 2000, Sminchisescu and Welling, 2011). For example, Mangoubi et al. (2018) show that, for multimodal target distributions, the ability of HMC to transition between modes is provably worse than that of random-walk Metropolis. We begin by providing an illustrative example that demonstrates the difficulty of HMC in exploring a multimodal distribution when π is a mixture of two Gaussian distributions.

Proposition 2.1. *For $d \geq 2$, let $\pi \propto 0.5 \mathcal{N}(-b\mathbf{1}_d, \mathbf{I}_d) + 0.5 \mathcal{N}(b\mathbf{1}_d, \mathbf{I}_d)$ be a bimodal target distribution, where $b > 0$. Let $\eta(t; \mathbf{z}_0) = \text{proj}_1 \circ \Phi_t(\mathbf{z}_0)$, i.e., $\eta(t; \mathbf{q}_0, \mathbf{p}_0) = \mathbf{q}_t$ where $(\mathbf{q}_t, \mathbf{p}_t) = \Phi_t(\mathbf{q}_0, \mathbf{p}_0)$, and let A_α be the high-density region around the mode $b\mathbf{1}_d$ given by*

$$A_\alpha = \left\{ \mathbf{q} \in \mathbb{R}^d : \|\mathbf{q} - b\mathbf{1}_d\| \leq \alpha\sqrt{d} \right\}.$$

Define $\mathcal{E}(b, d, \alpha)$ to be the event that the HMC transition kernel proposes a point $\eta(T; \mathbf{q}_0, \mathbf{p}_0)$ which is closer to $-b\mathbf{1}_d$ than $b\mathbf{1}_d$, i.e.,

$$\mathcal{E}(b, d, \alpha) = \left\{ \|\eta(T; \mathbf{q}_0, \mathbf{p}_0) + b\mathbf{1}_d\| \leq \|\eta(T; \mathbf{q}_0, \mathbf{p}_0) - b\mathbf{1}_d\|, \mathbf{q}_0 \in A_\alpha \right\}.$$

Then, for $b \geq \sqrt{\alpha^2 + 2\sigma^2}$,

$$\mathbb{P}\left(\mathcal{E}(b, d, \alpha)\right) \leq \exp\left(-\frac{d}{2}\left\{\frac{b^2 - \alpha^2}{2\sigma^2} - 1 - \log\left(\frac{b^2 - \alpha^2}{2\sigma^2}\right)\right\}\right). \quad (5)$$

The proof of Proposition 2.1 is provided in Appendix 6.1, and we make the following observations from the result.

Remark 2.2. *Although just an upper bound, Eq. (5) is useful for understanding the exponential decay of the transition probability as a function of the separation b and the dimension d .*

(i) *For simplicity, if we take $\alpha^2 = (1 - \delta)b^2$ for sufficiently small $\delta \in (0, 1)$, then the resulting term, $\delta b^2/\sigma^2$ in Eq. (5), effectively quantifies the energy barrier HMC needs to overcome to transition from the high-density region A_α near mode $b\mathbf{1}_d$, and propose a state closer to the mode $-b\mathbf{1}_d$. By applying the inequality, $x - 1 - \log(x) \geq (x - 1)^2/x$, it follows that the mode-transition probability bound in Eq. (5) decays exponentially with an increase in the energy barrier and the dimension d .*

(ii) *The condition that $b \geq \sqrt{\alpha^2 + 2\sigma^2}$ requires that the modes of π are sufficiently well-separated for the bound in Proposition 2.1 to hold. Indeed, if b was small, then the effective energy barriers between the modes would be small, and the effect of the multimodality of the target distribution would be negligible.*

(iii) *We note that it may be possible to obtain bounds similar to Eq. (5) for more general multimodal distributions by studying the conductance of the HMC algorithm for the target distribution π (Mangoubi et al., 2018). We also point out that the bound in Eq. (5) is different from Eq. (5) of Park (2021), which only provides a bound for transitioning between modes for a particular path in the HMC trajectory starting at one mode of the target distribution π .*

In order to address these shortcomings of HMC for multimodal target distributions, several methods have been proposed in the literature. As noted in Section 1, they can be, broadly, classified into the following three categories: (i) methods that generalize the original HMC dynamics to that of another physical system, (ii) methods which lower the energy barrier between modes by augmenting the phase-space via tempering

schemes or by introducing auxiliary variables, and (iii) methods that introduce a systematic method for identifying where the modes of the distribution are, and then adapting the HMC dynamics to jump between these modes.

In the first category, Tripuraneni et al. (2017) propose magnetic HMC where the HMC dynamics from classical mechanics is replaced by the Newtonian dynamics of a charged particle in a magnetic field. In essence, their method considers a non-canonical symplectic structure by replacing the lower-diagonal block of Ω in Eq. (2) with a user-specified invertible matrix \mathbf{R} . Brofos and Lederman (2020) extend this method to general non-canonical Hamiltonian systems by transforming the original phase space using the Darboux basis (Arnold, 2013, Chapter 8.43 B). Although these methods ensure that the resulting dynamics preserve $(\mathcal{P}1)$ – $(\mathcal{P}4)$, an appropriate choice of the matrices for the non-canonical Hamiltonian system remains an open question, and may be largely problem-specific.

In the second category, Betancourt (2014) proposes adiabatic Monte Carlo based on the principles of thermodynamics by replacing the symplectic structure with a contact structure (Arnold, 2013, Appendix 4). This results in a *contact Hamiltonian* defined on a $(2d + 1)$ -dimensional phase space given by

$$H_C(\mathbf{q}, \mathbf{p}, \eta) = \beta(\eta)U(\mathbf{q}) + K(\mathbf{p}) + (1 - \beta(\eta))V(\mathbf{q}) + \log Z(\beta(\eta)),$$

where $\eta \in \mathbb{R}$ governs a continuously varying (inverse) temperature $\beta(\eta) \in [0, 1]$. Roughly speaking, this temperature interpolates between the target π and a user-specified reference distribution $\varpi(\mathbf{q}) \propto \exp(-V(\mathbf{q}))$. Although theoretically appealing, practical implementation of the adiabatic Monte Carlo may be somewhat esoteric, and turns out to be infeasible in cases where the log-partition function $Z(\beta) = \int \pi(\mathbf{q})^\beta d\mathbf{q}$ is not known. Graham and Storkey (2017) and Luo et al. (2018) show that this issue can be, to some extent, ameliorated by using the approach of Gobbo and Leimkuhler (2015), i.e., by lifting the contact Hamiltonian to an *extended Hamiltonian* in a $(2d + 2)$ -dimensional phase space. Notwithstanding, an appropriate choice of the confining potential, V , and a suitable choice of the “conjugate momentum” for β are not entirely obvious. Park (2021), on the other hand, proposes tempered HMC based on a pre-specified mass scaling schedule $\{\Sigma_t : t \in \mathbb{R}\}$ for the mass matrix along the flow Φ_t . While the method performs well in exploring multimodal distributions, the time-varying mass schedule requires additional tuning, and, notably, doesn’t maintain the symplectic structure. On a different note, Nemeth et al. (2019) propose the pseudo-extended HMC where the target distribution is a product of the original $\pi(\mathbf{q})$ and its tempered versions $\{\pi(\mathbf{q})^{\beta_1}, \dots, \pi(\mathbf{q})^{\beta_k}\}$, with the expectation that in the augmented phase-space \mathbb{R}^{2dk} , the modes are connected to each other and facilitates better mode exploration for HMC.

The third class of HMC variants for sampling from multimodal distributions carefully design methods for identifying the location of modes while sampling at the same time. The difference between these methods, broadly, lies in the way they identify the modes (inner optimization routines) and how this information is transmitted to the Markov chain which is sampling from the target distribution. For example, Sminchisescu and Welling (2011) propose the method in which the task of finding the modes and sampling within modes is integrated into a single framework. Lan et al. (2014) propose the Wormhole Monte Carlo whereby, instead of performing local moves, mode-transition is enabled by constructing a special Riemannian metric which accounts for the geometry of the original phase space *and* the location of the modes. Their method uses the Riemann manifold Hamiltonian Monte Carlo algorithm (Girolami and Calderhead, 2011) to generate proposals.

Although these methods excel at investigating multimodal distributions due to their specific design to overcome the limitations of Hamiltonian Monte Carlo (HMC), they come with a trade-off. Often, the additional tuning parameters and computational overhead they introduce might be unnecessary and harder to justify when sampling from simpler, unimodal distributions. As we point out in Section 4.4, our proposed

methodology demonstrates advantages for sampling from both unimodal and multimodal distributions, and requires just one additional tuning parameter in comparison to HMC.

3 Repelling-Attracting Hamiltonian Monte Carlo

With this background, in this section we introduce the proposed repelling-attracting Hamiltonian Monte Carlo (RAHMC) algorithm. We first describe the key ideas behind RAHMC in Section 3.1, and, in Section 3.2, we describe its implementation details and investigate its properties as a Markov chain Monte Carlo algorithm. Next, in Section 3.3 we explain the procedure for tuning the parameters of RAHMC, and briefly discuss extensions of RAHMC in Section 3.4.

3.1 Motivation

The key idea behind RAHMC stems from non-idealized Hamiltonian systems in the presence of dissipative, damping forces, e.g., friction, viscosity, etc., termed as *conformal Hamiltonian systems* (McLachlan and Perlmutter, 2001).

Adding friction dissipates energy. The dynamics of a particle in a linearly damped conformal Hamiltonian system is governed by the equation

$$\frac{d}{dt} \begin{pmatrix} \mathbf{q}_t \\ \mathbf{p}_t \end{pmatrix} = \begin{bmatrix} \mathbf{O} & \mathbf{I} \\ -\mathbf{I} & \mathbf{O} \end{bmatrix} \begin{pmatrix} \nabla U(\mathbf{q}_t) \\ \nabla K(\mathbf{p}_t) \end{pmatrix} - \begin{bmatrix} \mathbf{O} & \mathbf{O} \\ \mathbf{O} & \gamma \mathbf{I} \end{bmatrix} \begin{pmatrix} \mathbf{q}_t \\ \mathbf{p}_t \end{pmatrix}, \quad (6)$$

where $\gamma \geq 0$ is a damping constant, which, in the case of classical mechanical systems, is also called the *coefficient of friction*. Similar to Eq. (2), by taking $\mathbf{z}_t = (\mathbf{q}_t, \mathbf{p}_t)$ to represent the state of the particle in the extended phase space, we can succinctly rewrite Eq. (6) as

$$\frac{d}{dt} \mathbf{z}_t = \Omega \nabla_{\mathbf{z}} H(\mathbf{z}_t) - \Gamma \mathbf{z}_t, \quad \text{where } \Gamma := \begin{bmatrix} \mathbf{O} & \mathbf{O} \\ \mathbf{O} & \gamma \mathbf{I} \end{bmatrix}. \quad (7)$$

When $\gamma = 0$, the dynamics of the conformal Hamiltonian system reduces to that of the conservative Hamiltonian system in Eq. (1). On the other hand, when $\gamma > 0$, the friction inhibits the motion of a particle since $d\mathbf{p}_t/dt = \nabla U(\mathbf{q}_t) - \gamma \mathbf{p}_t$. In contrast to the interpretation of conservative Hamiltonian dynamics in Neal (1996) as that of a hockey puck sliding over a frictionless surface, the conformal Hamiltonian dynamics in Eq. (7) can be interpreted as a dynamics associated with the same puck on a rough surface, thereby dissipating energy.

The dynamics of a particle under a conformal Hamiltonian vector field encourages the particle to *flow towards* the critical points of $U(\mathbf{q})$; this insight is used by França et al. (2020) to shed light on momentum-based optimization procedures such as Polyak’s heavy ball method, Nesterov’s accelerated-gradient method, and other alternatives. On a different note, Chen et al. (2014) incorporate a friction term in their proposal of stochastic-gradient HMC in order to establish invariance of the target distribution.

Subtracting friction accrues energy. If we depart from the physical analogy of Hamiltonian dynamics and consider the dynamics of a particle with an *amplifying* force,

$$\frac{d}{dt} \mathbf{z}_t = \Omega \nabla_{\mathbf{z}} H(\mathbf{z}_t) + \Gamma \mathbf{z}_t, \quad (8)$$

where, in contrast to Eq. (7), the additive term $\Gamma \mathbf{z}_t$ in Eq. (8) leads to an accrual of energy. The key observation is that, the *negative coefficient of friction* (owing to the $+\gamma \mathbf{p}_t$ term) amplifies the motion of a

particle, and the dynamics in Eq. (8) encourages the particle to *flow away* from the critical points of $U(\mathbf{q})$. Unlike the conservative and conformal Hamiltonian dynamics that have intuitive analogues to hockey pucks moving on frictionless or rough surfaces (i.e., preserving or dissipating energy), respectively, the amplifying Hamiltonian system does not have a physical analogue since the physical system is accruing energy as it moves.

For $t > 0$, let $\Phi_t^-, \Phi_t^+ : \mathbb{R}^{2d} \rightarrow \mathbb{R}^{2d}$ be the integral operators solving Eq. (7) and Eq. (8) for time t , respectively. The following lemma provides a formal justification for the interpretation of the dynamics in Eq. (8) and Eq. (7) as repelling and attracting dynamics, respectively.

Lemma 3.1. *Let $H(\mathbf{z}) = H(\mathbf{q}, \mathbf{p}) = U(\mathbf{q}) + \frac{1}{2}\mathbf{p}^\top \Sigma^{-1}\mathbf{p}$, then the time evolution of the Hamiltonian for Eq. (7) and Eq. (8), respectively, is given by*

$$\frac{d}{dt}H(\mathbf{z}_t) = \begin{cases} +\gamma \cdot \mathbf{p}_t^\top \Sigma^{-1}\mathbf{p}_t & \text{if } \mathbf{z}_t = \Phi_t^+(\mathbf{z}_0), \\ -\gamma \cdot \mathbf{p}_t^\top \Sigma^{-1}\mathbf{p}_t & \text{if } \mathbf{z}_t = \Phi_t^-(\mathbf{z}_0). \end{cases}$$

Notably, for $\mathbf{z}_t = \Phi_t^-(\mathbf{z})$, the Hamiltonian $H(\mathbf{z}_t)$ is a Lyapunov stable function (Sastry, 2013, Theorem 5.16), and all flows $\{\Phi_t^-(\mathbf{z}) : t > 0\}$ will tend to critical points $\mathbf{z}^* = (\mathbf{q}^*, \mathbf{p}^*)$ satisfying $\nabla \log \pi(\mathbf{q}^*) = 0$ and $\mathbf{p}^* = \mathbf{0}$. In contrast, for $\mathbf{z}_t = \Phi_t^+(\mathbf{z})$ the same critical points \mathbf{z}^* become *unstable*, i.e., the flows $\{\Phi_t^+(\mathbf{z}) : t > 0\}$ will tend to move away from \mathbf{z}^* . Lemma 3.1 is a well-known result for Hamiltonian systems with linear dissipation, and the proof is provided in Appendix 6.2 for completeness.

Example 3.1 (Bivariate Anisotropic Gaussian Mixture). *Let $\pi(\mathbf{q})$ be a bivariate Gaussian mixture given by*

$$\pi(\mathbf{q}) = 0.5\mathcal{N}_2(\mathbf{q} \mid \boldsymbol{\mu}, \Sigma_1) + 0.5\mathcal{N}_2(\mathbf{q} \mid -\boldsymbol{\mu}, \Sigma_2),$$

where $\boldsymbol{\mu} = (3, 3)^\top$, and

$$\Sigma_1 = \begin{bmatrix} 1.0 & 0.5 \\ 0.5 & 1.0 \end{bmatrix}, \quad \text{and} \quad \Sigma_2 = \begin{bmatrix} 1.0 & -0.5 \\ -0.5 & 1.0 \end{bmatrix}.$$

Figure 2(a) contrasts the conservative Hamiltonian dynamics (in green), from the conformal Hamiltonian dynamics of Eq. (7) (in blue). For two trajectories starting at the same initial position, the conformal Hamiltonian dynamics in Eq. (7) encourages the particle to flow towards the isolated modes of π , whereas the conservative Hamiltonian dynamics in Eq. (2) traverses the iso-energy contours of π .

In contrast, flipping the sign of the friction parameter γ transforms the attracting states into repelling states, and the trajectory of the particle under the amplifying Hamiltonian dynamics in Eq. (8) (in orange) traverses up the energy level-sets, as shown in Figure 2(b).

3.2 The proposed repelling-attracting Hamiltonian Monte Carlo algorithm

Although conformal Hamiltonian systems present an interesting perspective for studying the modalities of the target distribution, neither of them, by themselves, are suitable for sampling from multimodal distributions since they no longer retain the key properties, $(\mathfrak{P}3)$ – $(\mathfrak{P}4)$, which make the original Hamiltonian Monte Carlo successful in practice.

The RAHMC algorithm combines the repelling dynamics in Eq. (8) with the attracting dynamics in Eq. (7) to propose the next state of the Markov chain, which is followed by a Metropolis-Hastings filter. Specifically, for a time $T > 0$ and $\mathbf{z}_t = (\mathbf{q}_t, \mathbf{p}_t)$, the RAHMC dynamics is given by:

$$\frac{d}{dt}\mathbf{z}_t = \begin{cases} \boldsymbol{\Omega}\nabla_{\mathbf{z}}H(\mathbf{z}_t) + \boldsymbol{\Gamma}\mathbf{z}_t, & 0 < t \leq \frac{T}{2}, & (9a) \\ \boldsymbol{\Omega}\nabla_{\mathbf{z}}H(\mathbf{z}_t) - \boldsymbol{\Gamma}\mathbf{z}_t, & \frac{T}{2} < t \leq T. & (9b) \end{cases}$$

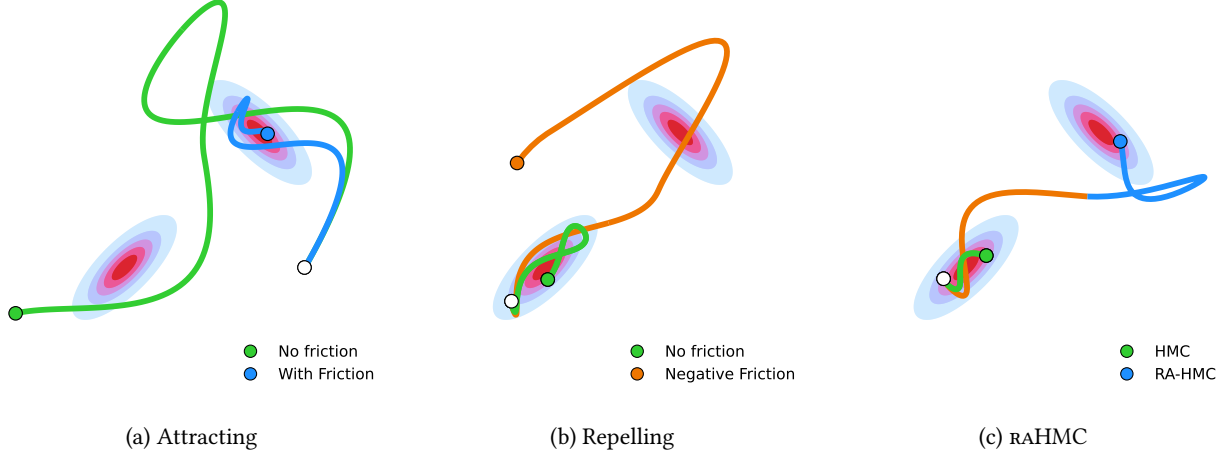


Figure 2: The dynamics of a particle starting at $\mathbf{q} \in \mathbb{R}^2$ (denoted by \circ). The first panel (a) shows a particle transition under the conservative Hamiltonian dynamics (ending up with \bullet) in Eq. (2) for fixed ϵ, L with initial momentum $\mathbf{p}_1 \in \mathbb{R}^2$, and that under the conformal Hamiltonian dynamics (ending up with \bullet) in Eq. (7) with $\gamma > 0$ and the same parameters ϵ, L . The particle under the conformal Hamiltonian dynamics with positive friction tends to be attracted to a nearby mode, unlike the one under the conservative Hamiltonian dynamics (no friction). The middle panel (b) displays the conservative Hamiltonian dynamics (\bullet) and amplifying Hamiltonian dynamics (\bullet) of Eq. (8) for fixed ϵ, L and $\mathbf{p}_2 \in \mathbb{R}^2$. Unlike the conservative Hamiltonian dynamics (no friction), the amplifying Hamiltonian dynamics (with negative friction) encourages a mode-repelling behavior of the particle. The last panel (c) exhibits a particle transition of RAHMC that combines the repelling and attracting dynamics ($\bullet + \bullet$), first being repelled from a local mode and then attracted to another mode.

For $\mathbf{z} = \mathbf{z}_0$ at time $t = 0$, the position of the particle at time $t = T$ in the extended phase space is given by

$$\mathbf{z}_T = \Psi_T := \Phi_{T/2}^- \circ \Phi_{T/2}^+(\mathbf{z}),$$

and, the final RAHMC proposal, $\tilde{\mathbf{z}}_T = \mathbf{F}(\mathbf{z}_T)$, after a momentum flip operation, is then accepted/rejected with probability

$$\alpha(\tilde{\mathbf{z}}_T | \mathbf{z}) = \min \left\{ 1, \exp \left(H(\tilde{\mathbf{z}}_T) - H(\mathbf{z}) \right) \right\}. \quad (10)$$

In the first half of the trajectory, the particle is driven away from its current mode by implementing the mode-repelling dynamics of Eq. (9a). Following this, in the second half of the trajectory, the particle is pulled towards a potentially new mode by the mode-attracting dynamics, as per Eq. (9b). This sequence of repulsion and attraction allows for better exploration of the modes of the target distribution. For the same target distribution from Example 3.1, Figure 2 (c) illustrates the RAHMC dynamics, where the particle is first repelled from the current mode and then attracted to another mode.

Remark 3.1. *We make some key observations about the RAHMC algorithm.*

(i) *The Repelling-Attracting Metropolis (RAM) algorithm proposed by Tak et al. (2018) shares a similar philosophy of combining repelling and attracting dynamics to sample from multimodal distributions. However, unlike the RAM algorithm, which is the repelling-attracting variant of random walk Metropolis-Hastings algorithm, RAHMC is based on Hamiltonian Monte Carlo. The key benefits of the proposed approach are: (a) eliminating the need for forced-transitions via repeated sampling in low-density regions (Tak et al., 2018, Table 1, Step 2), and (b) better adapting to the geometry of $\text{supp}(\pi)$, and thereby ensuring more efficient sampling from high-dimensional multimodal distributions. For detailed comparisons and results, please refer to the experiments in Section 4.*

(ii) In light of Lemma 3.1, the RAHMC dynamics, promotes transitions among a broader class of “modes” compared to those typically discussed in the MCMC literature. In \mathbb{R}^d and for $k \leq d$, the “generalized modes” of π could be interpreted as k -dimensional submanifolds of $\text{supp}(\pi)$ where $\nabla \log \pi(\mathbf{q}) = 0$. Several existing multimodal MCMC samplers (e.g., Lan et al., 2014, Pompe et al., 2020), are constructed to simulate transitions between isolated points in $\text{supp}(\pi)$, where $\log \pi(\mathbf{q})$ reaches a local maximum. These points correspond to the 0-dimensional modes of π . In contrast, according to Lemma 3.1, RAHMC facilitates transitions between these generalized modes of π , which includes, in particular, the 0-dimensional modes. Refer to Section 4.2 for an instance where RAHMC efficiently samples from π when the modes are 1- and 2-dimensional submanifolds of the ambient space.

The numerical implementation of the scheme in Eq. (9) is based on the *conformal leapfrog integrator* (Modin and Söderlind, 2011, Algorithm 3.1 and França et al., 2020, Eq. 3.3). For a step-size $\epsilon \approx dt$, the conformal leapfrog integrator for Eq. (9a) is given by the Strang splitting

$$\Phi_\epsilon^+ = \xi_{\epsilon/2}^\Gamma \circ \Phi_\epsilon^H \circ \xi_{\epsilon/2}^\Gamma, \quad (11)$$

where Φ_ϵ^H is the usual leapfrog step for the conservative Hamiltonian dynamics from Eq. (4), and $\xi_{\epsilon/2}^\Gamma(\mathbf{z}) = \xi_{\epsilon/2}^\Gamma(\mathbf{q}, \mathbf{p}) = (\mathbf{q}, e^{\gamma\epsilon/2}\mathbf{p})$ is the exact flow associated with the vector field $d\mathbf{z}_t/dt = \Gamma\mathbf{z}_t$. Mutatis mutandis, the integrator for Eq. (9b) is obtained by negating the sign of Γ , and is given by

$$\Phi_\epsilon^- = \xi_{\epsilon/2}^{-\Gamma} \circ \Phi_\epsilon^H \circ \xi_{\epsilon/2}^{-\Gamma}.$$

At time $T = L/\epsilon$, the position of \mathbf{z}_T in the extended phase-space is given by applying Φ_ϵ^+ repeatedly $\lfloor L/2 \rfloor$ times followed by Φ_ϵ^- repeatedly $\lfloor L/2 \rfloor$ times, i.e.,

$$\mathbf{z}_T = \Psi_{\epsilon,T}(\mathbf{z}) = \Phi_{\epsilon,L/2}^- \circ \Phi_{\epsilon,L/2}^+(\mathbf{z}) = (\Phi_\epsilon^-)^{\lfloor L/2 \rfloor} \circ (\Phi_\epsilon^+)^{\lfloor L/2 \rfloor}(\mathbf{z}). \quad (12)$$

An algorithmic description of the RAHMC transition is provided in Algorithm 1.

Remark 3.2. *The objective of Algorithm 1 is to first repel the particle from the current mode and then attract it to another mode, thereby encouraging better sampling from multimodal distributions. At time $T/2$, the dynamics of the particle transitions from mode-repelling to mode-attracting behavior. Mode exploration can be further encouraged by gently nudging the particle from backtracking to the same mode using the reflection principle (Neal, 2003, Eq. 12). In particular, at time $T/2$ (i.e., after Line 7 of Algorithm 1), the transformation*

$$R^\perp(\mathbf{q}, \mathbf{p}) = \left(\mathbf{q}, \mathbf{p} - 2\nabla U(\mathbf{q}) \left\langle \mathbf{p}, \frac{\nabla U(\mathbf{q})}{\|\nabla U(\mathbf{q})\|^2} \right\rangle \right),$$

reflects the momentum \mathbf{p} across the hyperplane orthogonal to the gradient of the potential energy $U(\mathbf{q})$, akin to a billiard ball bouncing off a wall. In our experiments, we observed that even without the reflection principle, RAHMC is able to explore multiple modes of the target distribution efficiently, and the reflection principle is not necessary for the RAHMC algorithm to work.

In order to establish that Algorithm 1 constitutes a valid Markov chain Monte Carlo algorithm, we turn our attention to investigate the properties of the RAHMC dynamics. We begin by describing a time-reversal symmetry property of Eq. (9). Following the convention in Lamb and Roberts (1998), for a dynamical system $d\mathbf{z}_t/dt = F(\mathbf{z}_t)$ with forward-time flow map $\Upsilon_t : \mathbf{z}_s \mapsto \mathbf{z}_{s+t}$, a map R is defined to be a *reversing symmetry* if $\Upsilon_t(R(\mathbf{z})) = R(\Upsilon_t^{-1}(\mathbf{z}))$, i.e., the forward-time flow of Υ_t after applying R is the same as R applied to the backward-time flow of Υ_t . The following result establishes a time-reversal symmetry between Φ_t^+ and Φ_t^- .

Algorithm 1: The Repelling-Attracting Hamiltonian Monte Carlo (RAHMC) algorithm.

Input : Potential $U := -\log \pi$, mass matrix $\Sigma \succ \mathbf{0}$, friction $\gamma > 0$, step size $\epsilon > 0$, length $L > 0$, sample size $N \in \mathbb{Z}_+$.

Output : Samples $\{q_1, q_2, \dots, q_N\} \subset \mathbb{R}^d$

Initialize $q_0 \in \mathbb{R}^d$ and **define** $H(\mathbf{q}, \mathbf{p}) := U(\mathbf{q}) + \frac{1}{2}\mathbf{p}^\top \Sigma^{-1}\mathbf{p}$;

```

1 for  $n = 1$  to  $N$  do
2   Sample  $\mathbf{p}_{n-1} \sim \mathcal{N}(\mathbf{0}, \Sigma)$ ;
3   Set  $(\mathbf{q}, \mathbf{p}) \leftarrow (\mathbf{q}_{n-1}, \mathbf{p}_{n-1})$ ;
4   for  $i = 1$  to  $\lfloor L/2 \rfloor$  do
5      $(\mathbf{q}, \mathbf{p}) \leftarrow \text{CONFORMAL-LEAPFROG}(\mathbf{q}, \mathbf{p}, \Sigma, \epsilon, -\gamma)$ ;
6   end
7   for  $i = 1$  to  $\lfloor L/2 \rfloor$  do
8      $(\mathbf{q}, \mathbf{p}) \leftarrow \text{CONFORMAL-LEAPFROG}(\mathbf{q}, \mathbf{p}, \Sigma, \epsilon, +\gamma)$ ;
9   end
10  Set  $(\mathbf{q}, \mathbf{p}) \leftarrow (\mathbf{q}, -\mathbf{p})$ ;
11  Set  $\alpha \leftarrow \min \{1, \exp(H(\mathbf{q}_{n-1}, \mathbf{p}_{n-1}) - H(\mathbf{q}, \mathbf{p}))\}$ ;
12  Sample  $u \sim \text{Unif}(0, 1)$ ;
13  if  $u < \alpha$  then
14     $q_n \leftarrow q$ ;
15  else
16     $q_n \leftarrow q_{n-1}$ ;
17  end
18 end
19 return  $\{q_1, q_2, \dots, q_N\}$ ;

20 Function  $\text{CONFORMAL-LEAPFROG}(\mathbf{q}, \mathbf{p}, \Sigma, \epsilon, \gamma)$ :
21    $\tilde{\mathbf{p}} \leftarrow e^{-\gamma\epsilon/2}\mathbf{p} - \frac{\epsilon}{2}\nabla U(\mathbf{q})$ ;
22    $\tilde{\mathbf{q}} \leftarrow \mathbf{q} + \epsilon\Sigma^{-1}\tilde{\mathbf{p}}$ ;
23    $\tilde{\mathbf{p}} \leftarrow e^{-\gamma\epsilon/2}(\tilde{\mathbf{p}} - \frac{\epsilon}{2}\nabla U(\tilde{\mathbf{q}}))$ ;
24   return  $(\tilde{\mathbf{q}}, \tilde{\mathbf{p}})$ 

```

Proposition 3.1. Let Φ_t^-, Φ_t^+ be the integral operators solving Eq. (7) and Eq. (8) for time t , respectively, and let $\mathbf{F} : (\mathbf{q}, \mathbf{p}) \mapsto (\mathbf{q}, -\mathbf{p})$ be the momentum-flip operator. Then,

$$\mathbf{F} \circ (\Phi_t^+)^{-1} = \Phi_t^- \circ \mathbf{F}, \quad \text{and} \quad \mathbf{F} \circ (\Phi_t^-)^{-1} = \Phi_t^+ \circ \mathbf{F} \quad \text{for all } t \in \mathbb{R}. \quad (13)$$

In particular, for the exact RAHMC flow operator Ψ_T and its numerical approximation $\Psi_{\epsilon,L}$, their compositions with the momentum-flip operator, $\mathbf{F} \circ \Psi_T$ and $\mathbf{F} \circ \Psi_{\epsilon,L}$, are involutions, i.e.,

$$(\mathbf{F} \circ \Psi_T) \circ (\mathbf{F} \circ \Psi_T) = \text{id} = (\mathbf{F} \circ \Psi_{\epsilon,L}) \circ (\mathbf{F} \circ \Psi_{\epsilon,L}).$$

In other words, Proposition 3.1 states that the momentum-flip operator $\mathbf{F}(\mathbf{q}, \mathbf{p}) = (\mathbf{q}, -\mathbf{p})$ relates the forward-time flow of Φ_t^\pm with the backward-time flow of Φ_t^\mp . When $\mathbf{F} \circ \Psi_T$ is composed with itself, momentum-flip operation helps undo the forward-time flow along Φ_T^- , but leaves the momentum flipped in this intermediate state. The flow along Φ_T^- from this intermediate state, now, reverses the forward-time

flow along Φ_T^+ . Therefore, from Tierney (1994), this guarantees that the resulting deterministic Markov kernel $z \mapsto \mathbf{F} \circ \Psi_T(z)$ satisfies the detailed-balance condition. The proof of Proposition 3.1 is provided in Section 6.3, and holds for Hamiltonians satisfying $H(\mathbf{q}, -\mathbf{p}) = H(\mathbf{q}, \mathbf{p})$.

Having established the reversibility of RAHMC, the following result shows that both Ψ_T and $\Psi_{\epsilon,L}$ preserve symplectic structure and volume in the extended phase space.

Proposition 3.2 (Preservation of Volume and Symplectic Structure). *Let ω_t be the symplectic 2-form given by the wedge product $\omega_t = d\mathbf{q}_t \wedge d\mathbf{p}_t$. Then, Eq. (9) preserves symplectic structure only when $t = T$, i.e.,*

$$\omega_T = \omega_0,$$

and, in particular, for all $z \in \mathbb{R}^{2d}$,

$$\mathbf{D}\Psi_T(z)^\top \Omega^{-1} \mathbf{D}\Psi_T(z) = \Omega^{-1}.$$

Moreover, the integrators Ψ_T and $\Psi_{\epsilon,L}$ are volume preserving, i.e., $|\det(\mathbf{D}\Psi_T)| = |\det(\mathbf{D}\Psi_{\epsilon,L})| = 1$.

As noted in (P2), preservation of volume in the phase space ensures that the Metropolis-Hastings acceptance probability does not require a correction term involving the Jacobian determinant. Hence, for $\tilde{z}_T = \mathbf{F} \circ \Psi_T(z)$ or $\tilde{z}_T = \mathbf{F} \circ \Psi_{\epsilon,L}(z)$, the proposed state \tilde{z}_T can be accepted/rejected with probability

$$\alpha(\tilde{z}_T | z) = \min \{1, \exp(H(\tilde{z}_T) - H(z))\}.$$

Propositions 3.1 and 3.2 alone are enough to guarantee that Algorithm 1 is a valid MCMC algorithm, and therefore, the samples generated by RAHMC are distributed according to the target distribution π . However, as noted in (P4) and (P3), the access to a symplectic integrator and the energy conservation of Hamiltonian dynamics ensure high acceptance probability, even over distant trajectories. To this end, the following result establishes that the numerical scheme for RAHMC, as described in Algorithm 1, is a second-order scheme and closely approximates the exact RAHMC dynamics.

Proposition 3.3 (Approximation Error). *For fixed $T = L\epsilon$, let Ψ_T be the exact time- T flow of the RAHMC dynamics in Eq. (9), and let $\Psi_{\epsilon,L}$ be the numerical scheme in Algorithm 1. Then,*

$$\|\Psi_{\epsilon,L}(z) - \Psi_T(z)\| = O(\epsilon^2), \quad \text{and} \quad \left| H(\Psi_{\epsilon,L}(z)) - H(\Psi_T(z)) \right| = O(\epsilon^2).$$

The proof of Proposition 3.3 is provided in Section 6.5, and the result is similar to the case of the conservative Hamiltonian dynamics when $T = L\epsilon$ is fixed. Therefore, for fixed T we don't sacrifice any numerical accuracy by departing to the conformal Hamiltonian framework. However, if T depends on ϵ , it can be shown via more involved and technical backward error analysis (see, e.g., Benettin and Giorgilli, 1994, Reich, 1999), that choosing $T_\epsilon = O(\epsilon^2 e^{C/\epsilon})$ guarantees the same $O(\epsilon^2)$ approximation error for H . This is not the case for RAHMC owing to the near-exponential growth of $H(\mathbf{q}_t, \mathbf{p}_t)$ in the repelling dynamics.

As far as energy conservation is concerned, the picture is more bleak; and the following result only guarantees an upper bound for the energy drift of the RAHMC dynamics. The result relies on some technical assumptions on the potential energy function $U(\mathbf{q})$, and, therefore, also on the target distribution π .

(A1) The negative log density $U(\mathbf{q}) = -\log \pi(\mathbf{q})$ is L -smooth, i.e., it is twice continuously differentiable and $\nabla U(\mathbf{q})$ is L -Lipschitz.

(A2) The Hessian $\nabla^2 U(\mathbf{q})$ is uniformly bounded, i.e., $\|\nabla^2 U(\mathbf{q})\| \leq \varpi$ for all $\mathbf{q} \in \mathbb{R}^d$.

(A3) $U(\mathbf{q})$ is coercive, i.e., $U(\mathbf{q}) \rightarrow \infty$ as $\|\mathbf{q}\| \rightarrow \infty$.

(A4) $U(\mathbf{q})$ is a Morse function, and

(A5) $U(\mathbf{q})$ satisfies the Polyak-Łojasiewicz condition, i.e., there exists a constant $\mu > 0$ such that for all critical points \mathbf{q}^* satisfying $\nabla U(\mathbf{q}^*) = 0$, the following inequality holds:

$$\|\nabla U(\mathbf{q})\|^2 \geq \mu \left(U(\mathbf{q}) - U(\mathbf{q}^*) \right).$$

With this background, the following result provides an upper bound for the energy drift of the RAHMC dynamics.

Proposition 3.4 (Bound on Energy Drift). *Suppose $U(\mathbf{q}) = -\log \pi(\mathbf{q})$ satisfies assumptions (A1)–(A5). For $T > 0$, let Ψ_T be the integral operator for the RAHMC dynamics, and let \mathcal{S} be the critical set of $H(\mathbf{z})$ given by*

$$\mathcal{S} := \left\{ (\mathbf{q}^*, \mathbf{0}_d) \in \mathbb{R}^{2d} : \nabla U(\mathbf{q}^*) = \mathbf{0}_d \right\}.$$

Then, the energy drift of the RAHMC dynamics is bounded by

$$\left| H(\Psi_T(\mathbf{z})) - H(\mathbf{z}) \right| \leq \inf_{\mathbf{u}, \mathbf{v} \in \mathcal{S}} \left| 2H(\Phi_{T/2}^+(\mathbf{z})) - H(\mathbf{u}) - H(\mathbf{v}) \right| e^{-\lambda T/2} + \sup_{\mathbf{u}, \mathbf{v} \in \mathcal{S}} \left| H(\mathbf{u}) - H(\mathbf{v}) \right|,$$

where $\lambda = \lambda(U, \Sigma, \gamma) > 0$ is a constant, given in Eq. (37), which depends only on U , Σ and γ .

The proof of Proposition 3.4 is presented in Appendix 6.6. While we are unable to guarantee that RAHMC conserves energy, the bound in Proposition 3.4 provides some control on the energy drift, and, in practice, we have observed that it is typically small. For example, Figure 3 shows the energy drift of RAHMC for random initial starting states \mathbf{z}_0 from the bivariate Gaussian mixture in Example 3.1 for different simulation lengths T , and different values of the friction parameter γ . Even for long trajectories, the energy drift is small as evidenced by the p -values in Figure 3. The practical implication of this is that, the optimal acceptance probability $\delta \in (0, 1)$ for RAHMC is likely to be smaller than that of HMC, which, under some strong assumptions, was shown to be $\delta \approx 0.651$ (Beskos et al., 2013).

Remark 3.3. *The proof of Proposition 3.4 is based on producing a Lyapunov function which decreases exponentially fast along the attracting stage of the RAHMC dynamics. Therefore, the assumptions (A1)–(A5) on $U(\mathbf{q})$ play a key role in establishing the bound on the energy drift. We make the following remarks about these assumptions.*

(i) *Assumptions (A1)–(A3) are standard in the literature on dynamical systems, control theory and optimization (e.g., Sastry, 2013, Polyak and Shcherbakov, 2018). In particular, (A1) guarantees that the trajectories are well-defined, and (A2) ensures that at each point the resulting dynamics are sufficiently well-behaved. The coercivity condition (A3) ensures that the level sets of the $H(\mathbf{q}, \mathbf{p})$ are bounded, and, therefore, compact. For $\pi(\mathbf{q})$, this requires the tails of π to not be thicker than the exponential distribution. Similar assumptions are also needed to guarantee the ergodicity of HMC (see, e.g., Livingstone et al., 2019).*

(ii) *Assumption (A4) is needed to ensure that the critical points in \mathcal{S} are isolated and non-singular. We note that this assumption is not restrictive, and it follows from the well-known result in Morse theory that Morse functions are dense in the space of smooth functions equipped with the uniform topology (Banyaga et al., 2004, Theorem 5.27).*

(iii) *Crucially, (A5) is needed to obtain quantitative bounds on the energy drift. The Polyak-Łojasiewicz condition ensures exponential convergence without the need for any assumptions on the convexity of $U(\mathbf{q})$. This allows for a more general class of target distributions, and, in particular, for multimodal distributions.*

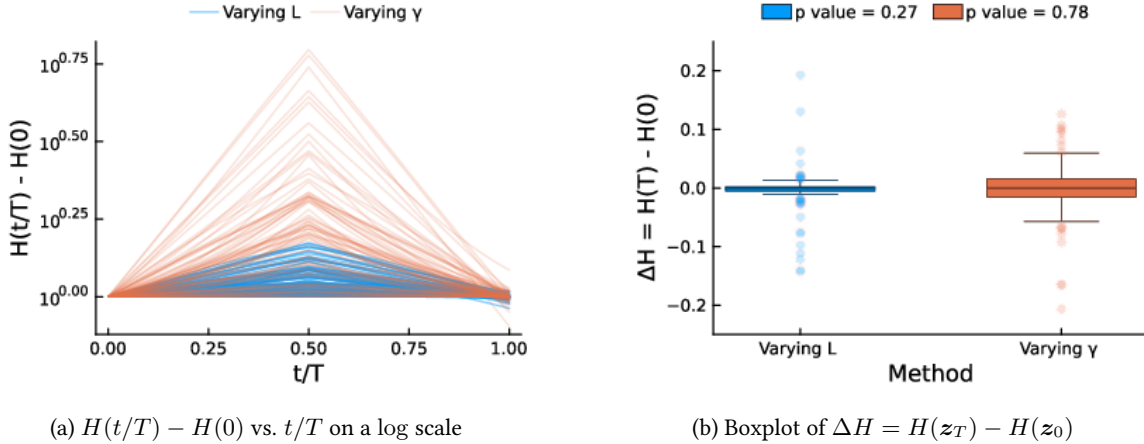


Figure 3: The energy drift of the RAHMC dynamics for random initial starting states z_0 from the bivariate Gaussian mixture in Example 3.1. For each of $N = 100$ trajectories, the step size $\epsilon = 10^{-3}$ is fixed, but the path length L (blue) and friction parameter γ (orange) are randomly sampled from $\text{Unif}\{1, 200\}$ and $\text{Unif}(0, 1)$, respectively. (Left) Plot of $H(z_t)$ for $N = 100$ trajectories where the X-axis, t/T , is normalized so as to depict all simulation lengths on a scale of $[0, 1]$. (Right) Boxplot of the energy drift $\Delta H = H(z_T) - H(z_0)$ for the same $N = 100$ trajectories. The p -values for the two-sided one-sample t -test for testing $\Delta H = 0$ vs. $\Delta H \neq 0$ shows insufficient statistical evidence that the energy drifts are statistically different from zero for randomly sampled T and γ .

3.3 Automatic tuning procedure for RAHMC via Nesterov dual-averaging

The success of RAHMC for sampling from multimodal distributions crucially hinges on the choice of the tuning parameters ϵ, γ, L . Specifically, Eq. (10) guarantees that RAHMC is able to overcome high energy barriers in the multimodal target distribution π by ascending iso-energy contours in the first half of the trajectory, Eq. (9a). In particular, if $\gamma > 0$ is sufficiently large, this can be achieved with relatively small total simulation length ϵL . On the other hand, if $\gamma > 0$ is very small, then the total simulation length ϵL must be large enough to overcome the high energy barriers.

Even for a given choice of γ and for an optimally tuned value of $T = \epsilon L$, the choice of ϵ is crucial for numerical stability. For instance, if the step size ϵ is too large, then, in very low density regions of the target distribution, $\log \pi(\mathbf{q}_{t+\epsilon}, \mathbf{p}_{t+\epsilon})$ can fall below machine precision and lead to numerical instability of the implementation. On the other hand, as is well-known to practitioners, if ϵ is too small then the effective computational cost of each RAHMC proposal can become prohibitively expensive.

Therefore, in order to address these concerns, we propose tuning these parameters using Nesterov dual-averaging (Nesterov, 2009) during the warm-up phase of the MCMC algorithm. This procedure has been shown by Hoffman and Gelman (2014) to be effective for tuning the parameters of both HMC and the No-U-Turn Sampler (NUTS). However, unlike the setting of HMC and NUTS, the tuning of RAHMC requires the additional tuning of the friction parameter γ .

To this end, let $\mathbf{x} = (\log \epsilon, \log \gamma) \in \mathbb{R}^2$, $\mathbf{g}_t(\mathbf{x}) \in \mathbb{R}^2$ be some statistic which measures the performance of RAHMC at time $t \in \mathbb{R}_+$, and let $\mathbf{G}(\mathbf{x}) = \mathbb{E}(\mathbf{g}_t|\mathbf{x}) = \lim_{T \rightarrow \infty} 1/T \sum_{t=1}^T \mathbf{g}_t(\mathbf{x})$ denote its expected value. Then, we can tune \mathbf{x} to minimize \mathbf{G} using the following update rule:

$$\begin{aligned} \mathbf{x}_{t+1} &\leftarrow \boldsymbol{\mu} - \frac{\sqrt{t}}{\omega} \frac{1}{t_0 + t} \sum_{i=1}^n \mathbf{g}_i \\ \bar{\mathbf{x}}_{t+1} &\leftarrow \eta_t \mathbf{x}_{t+1} + (1 - \eta_t) \bar{\mathbf{x}}_t, \end{aligned} \tag{14}$$

where \bar{x} is the dual-variable associated with x , $\boldsymbol{\mu} \in \mathbb{R}^2$ is a fixed-level that the parameters are shrunk towards, and $\omega > 0$ is a free parameter which controls the rate of shrinkage towards $\boldsymbol{\mu}$, $t_0 \geq 0$ controls the influence of the early iterations of the warm-up phase, and $\eta_t = t^{-k}$ for $k \in (0.5, 1]$ is a sequence of step-sizes. The main idea behind this tuning procedure is to view the statistic \mathbf{g}_t as the (sub-)gradient of a convex function, and then use the primal-dual averaging scheme (Nesterov, 2009) to tune the parameters x so as to find the zeros of the subgradient. This, loosely, corresponds to the minimization of a convex function. As noted in Hoffman and Gelman (2014), if the statistic \mathbf{g}_t is bounded, then sequence \bar{x}_t is guaranteed to converge to a value x^* such that $\mathbf{G}(x^*) = 0$.

Similar to the choice of the objective function for HMC in Hoffman and Gelman (2014, Section 3.2.3), we propose tuning the parameters γ and ϵ to achieve a desired Metropolis acceptance rate $\delta \in (0, 1)$. In particular, we choose

$$\mathbf{g}_i = \begin{pmatrix} f_i \\ f_i \end{pmatrix} \quad \text{for} \quad f_i := \delta - \min \left\{ 1, \exp \left(H(\Psi_{\mathbf{x}, T}(\mathbf{q}_i, \mathbf{p})) - H(\mathbf{q}_i, \mathbf{p}) \right) \right\},$$

where T is a fixed simulation length, $\mathbf{q}_{i-1} \in \mathbb{R}^d$ is the initial state, $\mathbf{p} \sim N(\mathbf{0}, \mathbf{I}_d)$ is the initial (resampled) momentum for the i -th iteration, and $\Psi_{\mathbf{x}, T}(\mathbf{q}_i, \mathbf{p})$ is the proposed state of the rAHMC trajectory in the i -th iteration using Eq. (9) with parameters $\epsilon = \exp(\text{proj}_1(\mathbf{x}))$, $\gamma = \exp(\text{proj}_2(\mathbf{x}))$ and $L = T/\epsilon$.

Under the same assumptions as Hoffman and Gelman (2014), i.e., if $\mathbb{E}(f_i | \mathbf{x})$ is monotone (non-increasing), it follows that $\mathbf{G}(\mathbf{x}) = \mathbb{E}(\mathbf{g}_i | \mathbf{x})$ is cyclically monotone, and can, therefore, be viewed as the (sub-)gradient of a convex function (Rockafellar, 1997, Theorem 24.8). Then, the tuning procedure in Eq. (14) can be used to exactly achieve a desired acceptance rate δ .

In all our experiments, we set $\delta \in \{0.55, 0.6\}$ and observed that we were able to roughly achieve the desired acceptance rate using the tuning procedure in Eq. (14). While the choice of $\delta = 0.65$ by Hoffman and Gelman (2014) for HMC is motivated by the optimal acceptance rate of HMC (under fairly strong assumptions), we note that a similar choice of δ for rAHMC warrants further investigation due to the energy drift in Eq. (3.4).

Since there are no systematic procedures for choosing the parameters ω, t_0, k in Eq. (14), we use the same values as in Hoffman and Gelman (2014) for HMC. In particular, we set $\omega = 0.05$, $t_0 = 10$, $k = 0.75$ and choose $\boldsymbol{\mu} = (\log(10\epsilon_0), \log(10\gamma_0))$, where ϵ_0 is set using Hoffman and Gelman (2014, Algorithm 4) and $\gamma_0 = 1.0$ is set to a reasonable value which enforces traversal *across* iso-energy contours of π . It is very likely that the optimal choice of these parameters for rAHMC will differ from their HMC and NUTS counterparts, but we have found them to be effective in practice, and leave the choice of these parameters as a topic for future research.

3.4 Extension to other variants of Hamiltonian Monte Carlo

In this section, we briefly highlight how the repelling-attracting dynamics of rAHMC can be incorporated into existing extensions of HMC. Lu et al. (2017) propose the Relativistic Monte Carlo algorithm, by considering the relativistic kinetic energy of the particle,

$$K'(\mathbf{p}) = m_0 c^2 \sqrt{1 + \frac{\mathbf{p}^\top \mathbf{p}}{m_0^2 c^2}},$$

where $m_0, c > 0$ are tunable parameters which represent the rest mass and the speed of light, respectively. For the Hamiltonian $H'(\mathbf{q}, \mathbf{p}) = U(\mathbf{q}) + K(\mathbf{p}')$,

$$\frac{d}{dt} \mathbf{z}_t = \boldsymbol{\Omega} \nabla_{\mathbf{z}} H'(\mathbf{q}_t, \mathbf{p}_t)$$

represents the dynamics of a particle z_t in a relativistic setting. In practice, this amounts to replacing $\mathbf{p} \sim \mathcal{N}(\mathbf{0}, \Sigma)$ with a symmetric hyperbolic distribution $\mathbf{p} \sim \pi(\mathbf{p} \mid m_0, c)$, and using the relativistic mass $M(\mathbf{p}) \in \mathbb{R}^{d \times d}$, the Relativistic Monte Carlo dynamics is equivalently given by

$$\frac{d}{dt} \mathbf{q}_t = M(\mathbf{p}_t)^{-1} \mathbf{p}_t, \quad \text{and} \quad \frac{d}{dt} \mathbf{p}_t = -\nabla U(\mathbf{q}_t).$$

This enables the Relativistic Monte Carlo algorithm to propose states using the leapfrog integrator. The rAHMC variant can be obtained by incorporating the repelling-attracting dynamics as follows:

$$\frac{d}{dt} \mathbf{q}_t = M(\mathbf{p}_t)^{-1} \mathbf{p}_t, \quad \text{and} \quad \frac{d}{dt} \mathbf{p}_t = -\nabla U(\mathbf{q}_t) - \text{sgn}(t - T/2) \gamma \mathbf{p}_t,$$

for $0 \leq t \leq T$. The numerical implementation of this dynamics is obtained by including the conformal Hamiltonian steps $\xi_\epsilon^\Gamma(\mathbf{q}, \mathbf{p}) = (\mathbf{q}, e^{\gamma\epsilon/2} \mathbf{p})$ before and after the leapfrog step in Lu et al. (2017, Section 2.1). In a similar vein, Tripuraneni et al. (2017) and Brofos and Lederman (2020) propose a variants of HMC whose dynamics are given by

$$\frac{d}{dt} \mathbf{z}_t = \underbrace{\begin{bmatrix} \mathbf{E} & \mathbf{A} \\ -\mathbf{A}^\top & \mathbf{G} \end{bmatrix}}_{=: \tilde{\Omega}(\mathbf{E}, \mathbf{G})} \nabla_{\mathbf{z}} H(\mathbf{z}_t), \quad (15)$$

where \mathbf{E}, \mathbf{G} are user-specified $d \times d$ skew-symmetric matrices which guarantee that $\tilde{\Omega}$ is a $2d \times 2d$ skew-symmetric matrix, and $\mathbf{A} \in \mathbb{R}^{d \times d}$ is fixed so as to ensure that $\tilde{\Omega}$ is invertible. This differs from the canonical dynamics in Eq. (2), and, notably, the proposals generated by Eq. (15) are not time-reversible in the classical sense. Instead, Eq. (15) satisfies a weaker form of time-reversibility (Tripuraneni et al., 2017), whereby negating the matrices \mathbf{E}, \mathbf{G} in addition to the momentum \mathbf{p} , i.e., $\tilde{\mathbf{F}}(\mathbf{z}, \mathbf{E}, \mathbf{G}) = (\mathbf{F}(\mathbf{z}), -\mathbf{E}, -\mathbf{G})$, is needed to obtain the time-reveral dynamics. This is similar to the pseudo time-reversibility of rAHMC as noted in Proposition 3.1, and this additional step is necessary to guarantee that the resulting proposal is an involution, and thereby satisfy the detailed balance condition.

Tripuraneni et al. (2017, Algorithm 1) proposes a sampler using a leapfrog-like integration scheme in the special case when $\mathbf{E} = \mathbf{0}$ and \mathbf{G} is a tunable-parameter for the sampler. Brofos and Lederman (2020, Algorithm 1) extends this idea to the case when, both, \mathbf{E} and \mathbf{G} , are tunable parameters, but relies on the implicit mid-point scheme in order to generate exact proposals from π . Although the choice of $\tilde{\Omega}$ is crucial for the success of these samplers, the repelling-attracting dynamics of rAHMC can be incorporated into these samplers in a straightforward manner:

$$\frac{d}{dt} \mathbf{z}_t = \begin{cases} \tilde{\Omega}(\mathbf{E}, \mathbf{G}) \nabla_{\mathbf{z}} H(\mathbf{z}_t) + \Gamma \mathbf{z}_t, & 0 < t \leq \frac{T}{2} \\ \tilde{\Omega}(\mathbf{E}, \mathbf{G}) \nabla_{\mathbf{z}} H(\mathbf{z}_t) - \Gamma \mathbf{z}_t, & \frac{T}{2} < t \leq T \end{cases}. \quad (16)$$

The exact implementation for the magnetic HMC framework can be obtained by adding an additional step before and after the leapfrog-like step in Tripuraneni et al. (2017, Algorithm 1) to account for the conformal Hamiltonian dynamics due to the $\pm \Gamma \mathbf{z}_t$ term in Eq. (16). A similar extension can be made to the non-canonical HMC framework of Brofos and Lederman (2020, Algorithm 1), and the exact details are beyond the scope of the current work. However, the key observation is that the repelling-attracting dynamics of rAHMC can be incorporated into these samplers in a straightforward manner, and can be made into valid MCMC algorithms.

4 Numerical Illustrations

In this section we examine the effectiveness of RAHMC in sampling from a variety of target distributions with multiple modes and complex geometry. We begin by describing the experimental setup and the target distributions used in the experiments.

Overview. In Section 4.1 we examine the effectiveness of the dual-averaging tuning scheme for RAHMC for a multivariate Gaussian mixture in varying dimensions. In Section 4.2, we compare the performance of RAHMC with four other MCMC methods on low-dimensional multimodal distributions with complex multimodal geometry, and in Section 4.3, we compare the same methods on high-dimensional target distributions. Lastly, in Section 4.4, we examine the advantage of RAHMC over standard HMC for sampling from unimodal distributions.

Methods. We compare the performance of RAHMC to four other MCMC methods. We use HMC with dual-averaging (Hoffman and Gelman, 2014, Algorithm 5) as the baseline to demonstrate improvement, if any. We use the Repelling-Attracting Metropolis algorithm (RAM, Tak et al., 2018) as a multimodal improvement of the random-walk Metropolis sampler, which requires no gradient information. In addition, we compare RAHMC to two improvements of HMC for multimodal distributions. The Wormhole HMC algorithm (WHMC, Lan et al., 2014) is used as an example of an HMC extension which stores the history of the chain to enable better mode exploration, and pseudo-extended HMC (PEHMC, Nemeth et al., 2019) is used as an example of a tempered HMC method which enables better mode transition in an extended phase-space \mathbb{R}^{2dk} of the original target distribution. In all cases, we run each MCMC method for 5,000 iterations after 1,000 iterations of warm-up.

Metrics. Throughout the numerical experiments, we evaluate the performance of each MCMC method based on three metrics: (i) the Sinkhorn distance, (ii) the average acceptance rate, and (iii) the CPU time in seconds. The average acceptance rate and the CPU time are used to measure the sampling and computational efficiency of the MCMC methods. The Sinkhorn distance is an entropic-regularized version of the Wasserstein distance (Cuturi, 2013) and is used as a quality measure for the resulting samples. In particular, we generate samples $\{\mathbf{q}_1, \mathbf{q}_2, \dots, \mathbf{q}_n\}$ from each of the MCMC methods, and, since we know how to sample from the exact target distribution for the examples here, we generate samples $\{\mathbf{q}'_1, \mathbf{q}'_2, \dots, \mathbf{q}'_n\} \sim \pi$. We evaluate the Sinkhorn distance between their empirical measures, $\mathbf{W}_2(\nu_n, \nu'_n)$, as a measure of sample quality. While this introduces some additional error from the empirical measure, ν'_n , we have found it to be a good metric for examining sample quality from multimodal distributions since the Wasserstein distance is intimately connected to the geometry of the target distribution, unlike other alternatives, e.g., the kernel Stein discrepancy. See, e.g., Panaretos and Zemel (2019) for an overview of the Wasserstein distance and its applications in statistics. In only the last example, where the target is a unimodal Gaussian distribution, we additionally compare auto-correlation functions (ACF). We do not compare ACFs in the multimodal examples since they can be misleading in distinguishing between Markov chains that are stuck in a local modes (Agarwal and Vats, 2022).

Hyperparameter tuning. In order to ensure that each method is properly tuned, we employ a number of techniques. For RAHMC, we use the procedure outlined in Section 3.3 to tune the parameters ϵ , γ , and L with $\delta \in \{0.55, 0.6\}$. For HMC, we use a similar dual-averaging approach to tune ϵ and L , with δ fixed at 0.6 (Hoffman and Gelman, 2014). For both RAHMC and HMC we select the expected simulation length, $\lambda = L\epsilon$ to ensure an acceptance probability between 40% and 80%. For the RAM algorithm, we use a Gaussian distribution with isotropic covariance $\sigma^2 \mathbf{I}_d$ as the proposal kernel, and we tune the value of σ^2 so that the acceptance rate is less than 90%. In some cases—particularly in higher dimensions—we report results of RAM with very low acceptance rates so as to avoid sticky samples. For PEHMC, similar to the experiments in Nemeth et al. (2019), we set the number of pseudo-samples, N , to be between 50 and

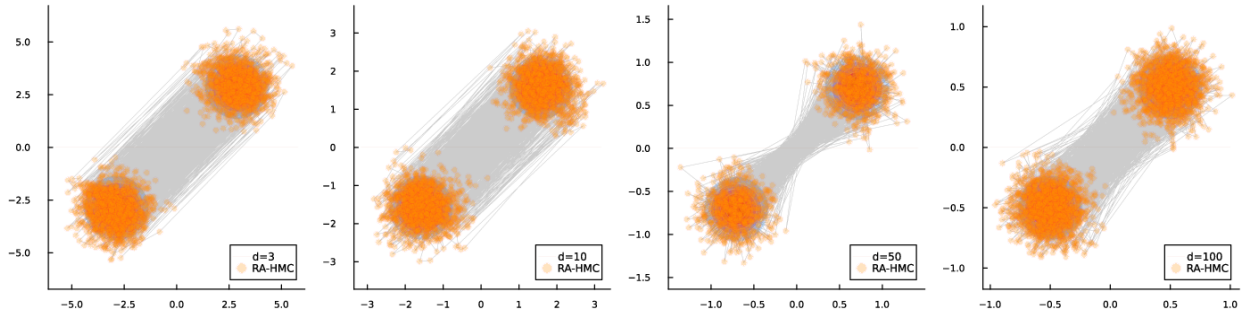


Figure 4: Results of parameter tuning for the RAHMC algorithm using dual averaging over $n = 10,000$ iterations for $d \in \{3, 10, 50, 100\}$. The scatterplots show the generated samples with gray lines indicating traces between consecutive samples.

Table 1: RAHMC with dual averaging ($\delta = 0.65$) for bimodal, isotropic Gaussian mixture.

Dimension	$d = 3$	$d = 10$	$d = 50$	$d = 100$
\mathbf{W}_2 metric	0.16	0.12	0.27	0.17
Acceptance Rate	63.9%	65.1%	36.7%	74.9%
CPU Time	27.9s	19.4s	1861.3s	7996.64s

200, and we tune the leapfrog parameters ϵ and L in order to obtain an acceptance rate greater than 40%. Finally, to tune WHMC we set the number of fixed-point steps to 10 and fix the *world distance* parameter and the influence factor for the mollifier at 1.0. We use an L-BFGS search with 100,000 max iterations for all regeneration routines. We also tune the leapfrog parameters ϵ and L , as well as the temperature T for the tempered residual potential energy of WHMC, to achieve an average acceptance rate greater than 40%.

4.1 Performance of dual averaging for RAHMC in high dimensions

In this experiment, we evaluate the performance of auto-tuning the RAHMC parameters ϵ, γ, L via dual averaging. The target distribution is a bimodal mixture of Gaussian distributions,

$$\pi(\mathbf{q}) \propto \mathcal{N}_d(\mathbf{x} \mid \boldsymbol{\mu}_1, \sigma^2 \mathbf{I}_d) + \mathcal{N}_d(\mathbf{x} \mid \boldsymbol{\mu}_2, \sigma^2 \mathbf{I}_d),$$

where $\boldsymbol{\mu}_1 = -\boldsymbol{\mu}_2 = (5/\sqrt{d})\mathbf{1}_d$ and the variance $\sigma^2 = 1/d$ are rescaled by the dimension. From Proposition 2.1, this effectively isolates the effect of increasing the dimension. For this example, the 2-Wasserstein metric between the target distribution π and any of its individual mixture components is a fixed value,

$$\mathbf{W}_2(\mathcal{N}_d(\boldsymbol{\mu}_1, \sigma^2 \mathbf{I}_d), \pi) = \mathbf{W}_2(\mathcal{N}_d(\boldsymbol{\mu}_2, \sigma^2 \mathbf{I}_d), \pi) = \frac{1}{\sqrt{2}} \|\boldsymbol{\mu}_1 - \boldsymbol{\mu}_2\|_2 \approx 7.07.$$

In particular, if a chain is stuck at a mode, the \mathbf{W}_2 metric is expected to be close to 7.07. The results from the auto-tuning RAHMC via dual-averaging are summarized in Table 1 and Figure 4. The results for the \mathbf{W}_2 metric in Table 1 are well below the threshold of 7.07, indicating that RAHMC discovers the two modes and that the samples are well-mixed even in \mathbb{R}^{100} . In Figure 4, the two-dimensional projections of the samples show that the sample RAHMC successfully makes frequent mode-jumping transitions.

4.2 Low dimensional examples

In this experiment, we compare the performance of each method on low-dimensional distributions with complex multimodal geometry, as shown in Figure 5. We consider the following four target distributions.

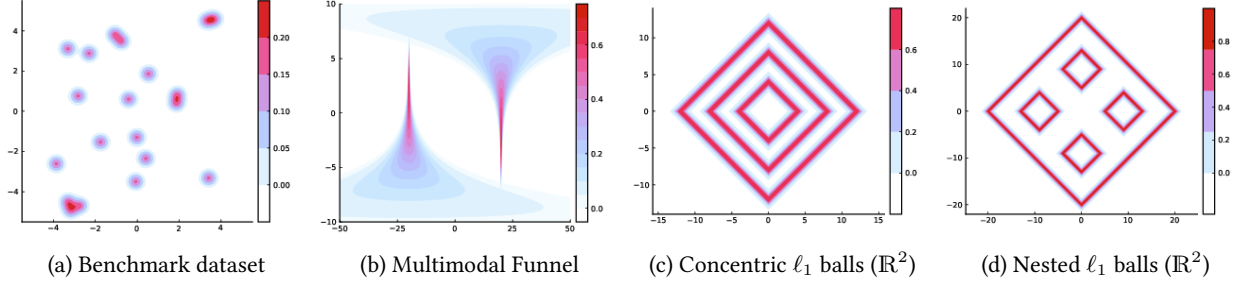


Figure 5: Ground truth for the low-dimensional target distributions in Section 4.2

Table 2: Results for Low dimensional examples from Section 4.2. Since the RAM algorithm does not make use of gradients, the information about the number of gradient evaluations L and that about the CPU time per each gradient evaluation are not available (denoted by NA).

Target	Method	W_2 metric	Acceptance Rate	# Gradients per step (L)	CPU Time per iteration (Time / L)
Benchmark	HMC	0.337	92.1%	27	24.2s (0.9s)
	RAHMC	0.011	57.4%	239	95.6s (0.4s)
	RAM*	0.025	22.1%	NA	1.8s (NA)
	PEHMC	0.152	56.7%	7	938.0s (134s)
	WHMC	0.051	84.3%	7	139.3s (19.9s)
Multimodal Funnel	HMC	26.823	42.7%	55	8.15s (0.15s)
	RAHMC	1.519	22.2%	5471	1094.00s (0.20s)
	RAM*	4.290	5.3%	NA	0.76s (NA)
	WHMC	27.383	94.9%	100	117.00s (1.17s)
Concentric ($d = 2$)	HMC	4.295	29.4%	27	10.8s (0.4s)
	RAHMC	0.191	63.2%	100	90.0s (0.9s)
	RAM*	0.407	43.8%	NA	1.1s (NA)
	PEHMC	4.418	84.6%	20	64.0s (3.2s)
	WHMC	4.233	60.0%	10	24.0s (2.4s)
Concentric ($d = 3$)	HMC	3.781	67.3%	45	22.5s (0.5s)
	RAHMC	0.647	52.8%	510	459.0s (0.9s)
	RAM*	1.618	27.9%	NA	0.1s (NA)
	PEHMC	21.640	79.4%	7	12.6s (1.8s)
	WHMC	19.696	86.1%	20	30.0s (1.5s)
Nested ($d = 2$)	HMC	14.088	90.3%	12	1.2s (0.1s)
	RAHMC	0.272	47.3%	61	12.2s (0.2s)
	RAM*	0.372	46.5%	NA	1.4s (NA)
	PEHMC	1.036	50.0%	20	150s (7.5s)
	WHMC	13.742	92.0%	10	24.0s (2.4s)
Nested ($d = 3$)	HMC	3.868	65.0%	289	28.9s (0.1s)
	RAHMC	1.159	63.7%	1655	165.5s (0.1s)
	RAM*	2.089	32.9%	NA	0.1s (NA)
	PEHMC	64.030	80.8%	20	120.0s (6.0s)
	WHMC	97.863	79.0%	25	25.0s (1.0s)

*Since the RAM algorithm is gradient-free, the total CPU time and total memory are reported.

(A) Benchmark Dataset. Our first example is a mixture of twenty bivariate Normal distributions with equal weight as the target distribution (Kou et al., 2006). The mixture is defined as

$$\pi(\mathbf{q}) \propto \sum_{j=1}^{20} \exp\left(-\frac{(\mathbf{q} - \mu_j)^\top (\mathbf{q} - \mu_j)}{2\sigma^2}\right)$$

for $\mathbf{q}^\top = (q_1, q_2) \in \mathbb{R}^2$ with $\sigma^2 = 0.01$. The mean vectors of the twenty components are available in Kou et al. (2006). The target distribution is plotted in Figure 5 (a).

(B) Multimodal Funnel. Our second example is a multimodal generalization of Neal’s funnel (Neal, 2003), and the 2-dimensional target distribution π is given by

$$\pi(q_1, q_2) = \pi_1(q_1|q_2, c, \mu) \times \pi_2(q_2|\mu, \sigma),$$

where $\pi(q_2|\mu, \sigma) \propto \mathcal{N}(\mu - 5, \sigma) + \mathcal{N}(\mu + 5, \sigma)$ and $\pi(q_1|q_2, c, \sigma) \propto \mathcal{N}(c, e^{c-\mu-q_2/2}) + \mathcal{N}(-c, e^{c-\mu-q_2/2})$. We set $\mu = 3, \sigma = c = 1$, and Figure 5 (b) displays the corresponding target distribution of (q_1, q_2) .

(C) Concentric ℓ_1 Balls. In our remaining examples, we consider target distributions with subtle geometric structures in addition to multimodality. The first of these is a mixture of distributions supported on the boundary of three *concentric* ℓ_1 balls in \mathbb{R}^d , and the target $\pi(\mathbf{q})$ is given by

$$\pi(\mathbf{q}) \propto \sum_{i=1}^3 \exp(-(\|\mathbf{q}\|_1 - r_i)^2/2\sigma^2),$$

where $r_1 = 4, r_2 = 8, r_3 = 16$ and $\sigma = 0.5$. We consider the cases when $d = 2$ and $d = 3$. See Figure 5 (c) for the target distribution in \mathbb{R}^2 .

(D) Nested ℓ_1 Balls. Our final example is a mixture of distributions supported on the boundary of *nested* ℓ_1 balls in \mathbb{R}^d . The target distribution, $\pi(\mathbf{q})$, is given by

$$\pi(\mathbf{q}) \propto \sum_{i=1}^5 \exp(-(\|\mathbf{q} - \mu_i\|_1 - r_i)^2/2\sigma^2),$$

where $\mu_1 = \mathbf{0}, r_1 = 20$, and $\|\mu_i\|_1 = 2, r_i = 2$ for $2 \leq i \leq 5$. Similar to example (C), we consider the cases when $d = 2$ and $d = 3$, and the target distribution when $d = 2$ is shown in Figure 5 (d).

The results for the experiment are summarized in Table 2. The results show that RAHMC outperforms the other methods in terms of the \mathbf{W}_2 metric for all the examples. This, however, comes at the price of a higher computational cost, as the auto-tuning procedure for RAHMC tends to favor longer trajectories, and therefore requires more gradient evaluations per step. RAM is able to achieve reasonably low \mathbf{W}_2 accuracy with better CPU time, but comes at the cost of low acceptance rates. This can be attributed to the forced mode transitions with a random-walk kernel (Tak et al., 2018, Eq. 3) which can lead to rejections when the target distribution is supported on lower dimensional structures. WHMC performs competitively when the $\pi(\mathbf{q})$ has well-separated and isolated modes, as in the benchmark dataset, but performs poorly when the modes of the target distribution are, in fact, entire submanifolds as is the case for examples (C) and (D).

The traceplots for the benchmark dataset in example (A) are displayed in Figure 6, and show that RAHMC is able to explore the twenty modes effectively and comes closest to the ideal sampling scenario. For the multimodal funnel in example (B), RAHMC and RAM are the only two algorithms that are able to move

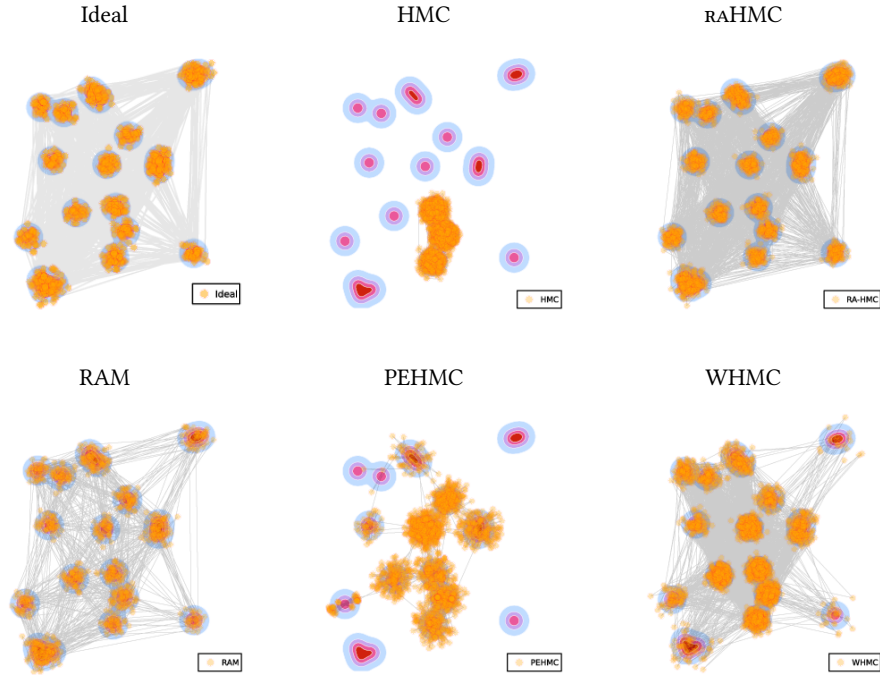


Figure 6: Trace plots of the last 1,000 iterations obtained by the five different MCMC samplers for the benchmark target distribution in Section 4.2 (A). The plot in the top-left corner shows the ideal trace plot if the sampler was able to explore all the modes.

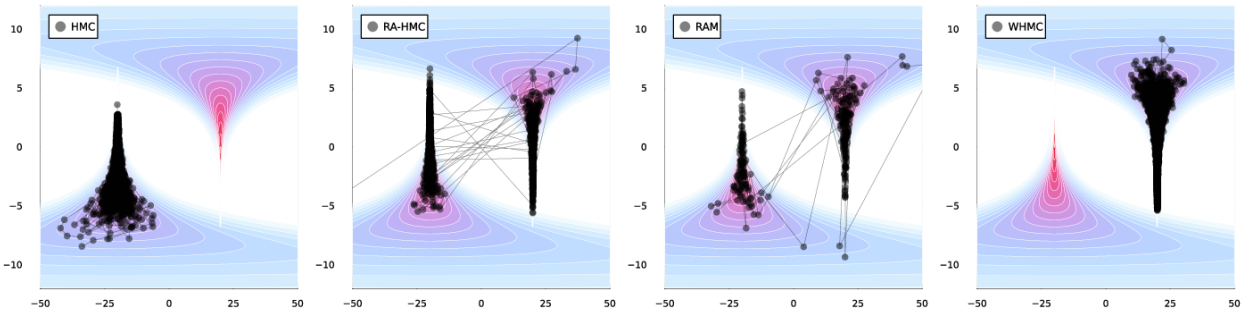


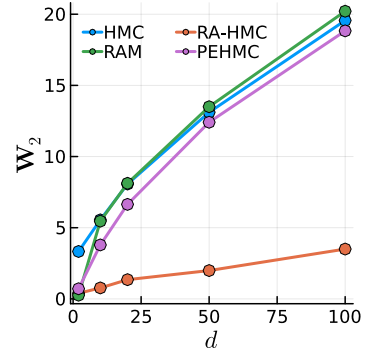
Figure 7: Scatterplots of the last 1,000 iterations obtained by four different samplers for the multimodal funnel distribution in Section 4.2. RAHMC and RAM are the only samplers that move between two modes. In particular, RAHMC samples the sharp tips of the funnels more accurately than RAM does.

between the two high-density regions, but RAHMC is able to sample the sharp tips of the funnels more accurately than RAM does, as shown in Figure 7.

The results for the concentric and nested ℓ_1 balls in examples (C) and (D) are shown in Figure 8. While both RAM and RAHMC are competitive when $d = 2$ and are able to discover and sample from the 1-dimensional modes effectively, increasing the dimension to $d = 3$ makes RAM less effective; in fact, the acceptance probability drops from 50% to 30%. When $d = 2$, HMC is able to move between two of the three generalized modes for the concentric ℓ_1 case, but is unable to move between the modes for the nested ℓ_1 case. WHMC is able to discover one of the high-density regions, but when the inner-optimization routine is run from an existing high-density region, it converges to the density ridge associated with the same ℓ_1 ball. Therefore, it is unable to discover or move between these generalized modes. PEHMC, on the other hand, performs well when $d = 2$, but when $d = 3$ it is unable to discover the modes of the target

Table 3: Summary of the sampling results obtained by four different sampling methods for the anisotropic Gaussian mixtures in Section 4.3. The figure on the right-hand side visualizes each method’s \mathbf{W}_2 values over dimensions. It shows how quickly the performance of the samplers can deteriorate when the dimension increases, while RAHMC maintains the quality of the resulting sample in a relatively stable manner.

	Method	$d = 2$	$d = 10$	$d = 20$	$d = 50$	$d = 100$
\mathbf{W}_2 metric	HMC	3.33	5.55	8.07	13.11	19.56
	RAHMC	0.39	0.77	1.35	1.99	3.50
	RAM	0.26	5.46	8.12	13.50	20.21
	PEHMC	0.71	3.79	6.64	12.41	18.83
Acceptance Rate	HMC	71.7%	82.8%	59.6%	91.1%	97.5%
	RAHMC	49.2%	65.7%	62.6%	67.2%	71.4%
	RAM	31.9%	11.8%	43.7%	29.1%	50.1%
	PEHMC	92.0%	63.6%	63.5%	88.5%	69.2%



distribution effectively. This may be, perhaps, attributed to the fact that PEHMC relies on the assumption that the cartesian product of the phase-space leads to intersections between different modes—which may not be the case for the nested ℓ_1 balls. It also likely, however, that a more careful tuning of the WHMC and PEHMC hyperparameters could lead to better performance; we were unable to find such a tuning in this work.

4.3 Anisotropic Gaussian Mixture in High Dimensions

In this experiment, we consider a generalization of the bivariate Gaussian mixture model from Example 3.1. For $\mathbf{q} \in \mathbb{R}^d$, the target distribution is

$$\pi(\mathbf{q}) = 0.5\mathcal{N}_d(\mathbf{q} \mid b\mathbf{1}_d, \Sigma_1) + 0.5\mathcal{N}_d(\mathbf{q} \mid -b\mathbf{1}_d, \Sigma_2),$$

where $b = 2$, and the covariance matrices are given by $[\Sigma_1]_{i,j} = 0.75^{|i-j|}$ for $i, j = 1, 2, \dots, d$ and $\Sigma_2 = 2\mathbf{I}_d - \Sigma_1$. We compare the performance of four MCMC methods when $d \in \{2, 10, 20, 50, 100\}$, and the results are summarized in Table 3. We omit the WHMC algorithm from this experiment as we were unable to find an appropriate tuning of the hyperparameters for high-dimensions. The covariance structure of the target distribution is particularly challenging for gradient based methods, as the principal eigenvectors of the covariance matrices are perpendicular to each other. RAHMC maintains the smallest \mathbf{W}_2 metric for all the dimensions except $d = 2$, and the acceptance rate is also stable across the dimensions. As seen in Section 4.2 RAM is able to achieve reasonably low \mathbf{W}_2 accuracy with better CPU time when $d = 2$. HMC and PEHMC also perform competitively when $d = 2$, but their performance deteriorates as the dimension increases.

4.4 Sampling from Unimodal Distributions

MCMC algorithms which are designed to sample from multimodal distributions are often bespoke for multimodal settings and are less efficient for sampling from unimodal distributions. While the previous experiments have shown that RAHMC is competitive for sampling from multimodal distributions, in this experiment we demonstrate that RAHMC demonstrates improvement over HMC for sampling from unimodal distributions. We consider the problem of sampling from a standard d -dimensional Gaussian distribution, $\mathcal{N}(\mathbf{0}, \mathbf{I}_d)$, and compare the performance of RAHMC and HMC for $d \in \{2, 10, 50, 100\}$. For both HMC and RAHMC, we set $\epsilon = 0.5$ and $L = 20$, and we draw samples of size 10,000 (with the first 5,000 as warm-up). Additionally, for RAHMC we set $\gamma = 0.05$. Therefore, any differences in the performance of the two methods can be purely attributed to the repelling-attracting dynamics introduced by the parameter γ .

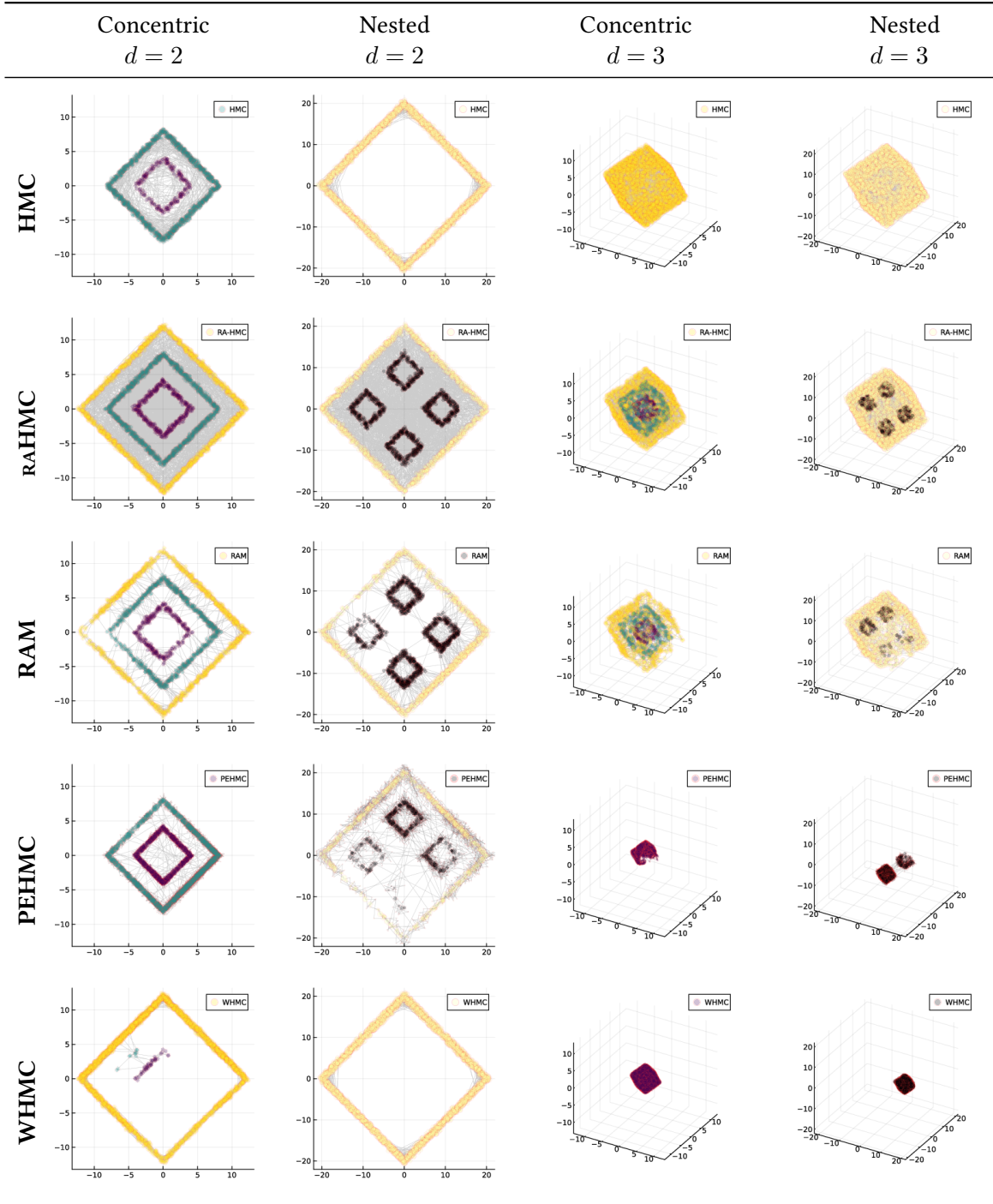


Figure 8: Scatterplots of the last 1,000 iterations obtained by five different samplers for the concentric and nested ℓ_1 balls in both $d = 2$ and $d = 3$ in Section 4.2. RAHMC and RAM are the only samplers that capture the lower dimensional submanifold structure in addition to multimodality. Although the sampling quality of RAM deteriorates noticeably in $d = 3$, that of RAHMC is stable regardless of the dimension.

The results in Table 4 present the quality of the last 5,000 samples obtained from HMC and RAHMC in terms of the \mathbf{W}_2 metric and its expected margin of error of $\approx n^{-1/d}$ (Fournier and Guillin, 2015) is provided in the last row of Table 4 for reference. Notably, there is no significant difference in sample quality between

Table 4: W_2 metric for sampling from unimodal, isotropic Gaussian distribution

Method	$d = 3$	$d = 10$	$d = 50$	$d = 100$
HMC	0.17	3.10	53.41	133.09
RAHMC	0.19	3.23	54.72	136.05
Margin of error	0.06	0.43	0.84	0.92

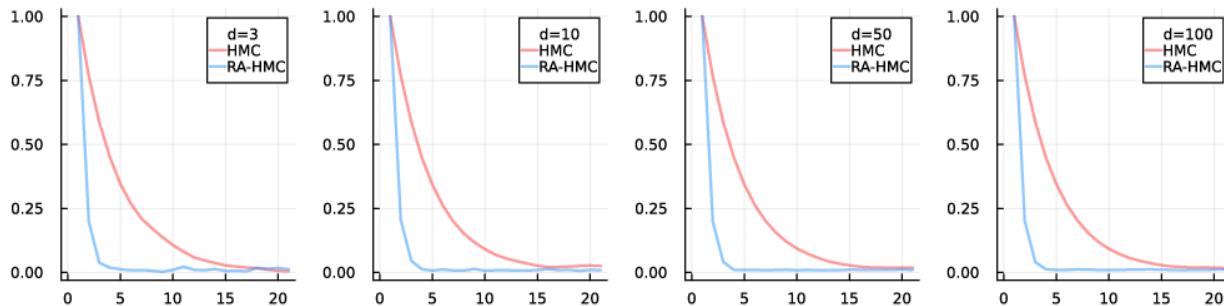


Figure 9: Autocorrelation functions of HMC’s and RAHMC’s samples for the standard unimodal, isotropic Gaussian distributions with $d \in \{3, 10, 50, 100\}$.

the two methods. Since ϵ and L are the same for both methods, the CPU time for both methods is also roughly the same.

On the other hand, the autocorrelation functions of the last 5, 000 samples (and for the first coordinate) of the Markov chain are shown in Figure 9. Notably, in all dimensions RAHMC leads to considerably better mixing than HMC. This can be explained by the fact that, as per Eq. (9a), the first half of the RAHMC trajectory is essentially simulating a *chaotic dynamical system* where the modes of the target distribution are Lyapunov unstable states. This leads to better mixing of the samples, and substantially improves the expected sample size (ESS) without sacrificing the sample quality.

5 Concluding Remarks

In this work, we have proposed the repelling-attracting Hamiltonian Monte Carlo (RAHMC) as an enhancement of Hamiltonian Monte Carlo for sampling from high-dimensional target distributions with complex, multimodal structures. The key idea which distinguishes RAHMC from HMC is the introduction of the friction parameter, γ , which facilitates the movement *across* iso-energy contours to generate proposals. The RAHMC algorithm comprises of two stages: in the first stage, the high-density regions of the target distribution serve as repelling states, encouraging mode exploration; while in the second stage, the high-density regions serve as attracting states and forces to trajectory to settle near alternative modes. While this is achieved by departing from conservative Hamiltonian systems to the generalized conformal Hamiltonian systems, RAHMC is designed to preserve the target distribution and the underlying symplectic structure—properties which are key for the success of HMC. We have shown that RAHMC also retains the same numerical accuracy as HMC, while being able to generate Markov chains which lead to substantially better mixing. Lastly, we provided a procedure for automatically tuning the hyperparameters of RAHMC using the version of Nesterov dual-averaging proposed by Hoffman and Gelman (2014).

In Section 3.4 we discussed how the repelling-attracting idea underlying RAHMC can be extended to some other variants of HMC in literature. However, the benefit of such an extension has not been investigated in this article, and is an interesting direction for future research. Furthermore, the No-U-Turn Sampler (NUTS,

Hoffman and Gelman, 2014) is a popular variant of HMC which has been shown to be more efficient than HMC in many cases. It would be interesting to investigate the possibility of incorporating the repelling-attracting mechanism into NUTS, and the impact of such an extension. We point out, however, that in stark contrast to NUTS, we want to ensure that the trajectory generated by RAHMC makes a U-Turn when it transitions from the repelling to the attracting stage. Therefore, a direct application of the repelling-attracting mechanism to NUTS may not be straightforward. Lastly, we have not been able to guarantee that RAHMC conserves energy, although the energy drift can be bounded as shown in Proposition 3.4, and is able to maintain high acceptance probability even across distant trajectories, as evidenced by the numerical experiments in Section 4. A more detailed theoretical investigation of the energy preservation and the geometric ergodicity of RAHMC is left for future research.

6 Proofs

In this section, we provide the proofs of the main results in the paper.

6.1 Proof of Proposition 2.1

We begin by noting that the randomness in the event $\mathcal{E}(b, d, \alpha)$ arises solely from the initial momentum $\mathbf{p}_0 \sim \mathcal{N}(\mathbf{0}, \mathbf{I})$. With this in mind, let B be the hyperplane defined by

$$B = \left\{ \mathbf{y} \in \mathbb{R}^d : \|\mathbf{y} - b\mathbf{1}_d\| = \|\mathbf{y} + b\mathbf{1}_d\| \right\}, \quad (17)$$

and let B^- and B^+ be the half-spaces which are closer to $-b\mathbf{1}_d$ and $b\mathbf{1}_d$, respectively. Let $\mathcal{E}_1, \mathcal{E}_2$ be the events defined by,

$$\mathcal{E}_1 = \left\{ \mathbf{p}_0 : \frac{1}{2}\|\mathbf{p}_0\|^2 \geq \inf_{\mathbf{q} \in A_\alpha} \log \pi(\mathbf{q}) - \sup_{\mathbf{q} \in B} \log \pi(\mathbf{q}) \right\} \quad \text{and} \quad \mathcal{E}_2 = \left\{ \mathbf{p}_0 : \frac{1}{2}\|\mathbf{p}_0\|^2 \geq d \left(\frac{b^2 - \alpha^2}{4\sigma^2} \right) \right\}.$$

The proof proceeds in two steps:

1. We first show that $\mathcal{E}(b, d, \alpha) \subseteq \mathcal{E}_1 \subset \mathcal{E}_2$
2. We use a Chi-squared tail probability bound on $\mathbb{P}(\mathcal{E}_2)$ to obtain the desired result.

Step 1: For any $\mathbf{q}_0 \in A_\alpha$ and $\mathbf{p}_0 \in \mathcal{E}(b, d, \alpha)$, since $\mathbf{q}_0 \in B^+$ and $\eta(T; \mathbf{q}_0, \mathbf{p}_0) \in B^-$, and because $\Phi_t : \mathbb{R}^{2d} \rightarrow \mathbb{R}^{2d}$ is a smooth map for each t , it follows that there exists $t \in [0, T]$ such that $\eta(t; \mathbf{z}_0) \in B$. Therefore,

$$\begin{aligned} \mathbf{p}_0 \in \mathcal{E}(b, d, \alpha) &\implies \exists t \in [0, T] \quad \text{s.t.} \quad \eta(t; \mathbf{p}_0, \mathbf{q}_0) \in \mathcal{E}_1 \\ &\implies \exists t \in [0, T] \quad \text{s.t.} \quad H(\mathbf{q}_t, \mathbf{p}_t) \leq H(\mathbf{q}_0, \mathbf{p}_0), \quad \mathbf{q}_t \in B \\ &\implies \exists t \in [0, T] \quad \text{s.t.} \quad \frac{1}{2}\|\mathbf{p}_t\|^2 - \log \pi(\mathbf{q}_t) \leq \frac{1}{2}\|\mathbf{p}_0\|^2 - \log \pi(\mathbf{q}_0), \quad \mathbf{q}_t \in B \\ &\implies \exists t \in [0, T] \quad \text{s.t.} \quad \frac{1}{2}\|\mathbf{p}_0\|^2 \geq \log \pi(\mathbf{q}_0) - \log \pi(\mathbf{q}_t) + \frac{1}{2}\|\mathbf{p}_t\|^2, \quad \mathbf{q}_t \in B \\ &\implies \exists t \in [0, T] \quad \text{s.t.} \quad \frac{1}{2}\|\mathbf{p}_0\|^2 \geq \inf_{\mathbf{q} \in A_\alpha} \log \pi(\mathbf{q}) - \sup_{\mathbf{q} \in B} \log \pi(\mathbf{q}) + \frac{1}{2}\|\mathbf{p}_t\|^2 \end{aligned}$$

$$\begin{aligned} \therefore \mathbf{p}_0 \in \mathcal{E}(b, d, \alpha) &\stackrel{(i)}{\implies} \|\mathbf{p}_0\|^2 \geq \inf_{\mathbf{q} \in A_\alpha} \log \pi(\mathbf{q}) - \sup_{\mathbf{q} \in B} \log \pi(\mathbf{q}) \\ &\implies \mathbf{p}_0 \in \mathcal{E}_1, \end{aligned} \quad (18)$$

where the implication (i) follows from the fact that $\|\mathbf{p}_t\|^2 \geq 0$. Therefore, $\mathcal{E}(b, d, \alpha) \subseteq \mathcal{E}_1$. Furthermore, for $\pi(\mathbf{q})$ given by

$$\pi(\mathbf{q}) = \lambda \left\{ \exp\left(-\frac{1}{2\sigma^2} \|\mathbf{q} - b\mathbf{1}_d\|^2\right) + \exp\left(-\frac{1}{2\sigma^2} \|\mathbf{q} + b\mathbf{1}_d\|^2\right) \right\},$$

where $\lambda > 0$ is the normalizing constant of π , using the fact that $\log(x + y) > \log x$ for all $x, y > 0$, it follows that

$$\inf_{\mathbf{q} \in A_\alpha} \log \pi(\mathbf{q}) \geq \log \lambda - \sup_{\mathbf{q} \in A_\alpha} \frac{\|\mathbf{q} - b\mathbf{1}_d\|^2}{2\sigma^2} = \log \lambda - \frac{\alpha^2 d}{2\sigma^2}. \quad (19)$$

Similarly, using the fact that $\|\mathbf{q} - b\mathbf{1}_d\| = \|\mathbf{q} + b\mathbf{1}_d\|$ for all $\mathbf{q} \in B$, it follows that

$$\sup_{\mathbf{q} \in B} \log \pi(\mathbf{q}) \leq \log 2 + \log \lambda - \inf_{\mathbf{q} \in B} \frac{\|\mathbf{q} - b\mathbf{1}_d\|^2}{2\sigma^2} = \log 2 + \log \lambda - \frac{b^2 d}{2\sigma^2}. \quad (20)$$

For $\mathbf{p}_0 \in \mathcal{E}_1$, plugging in Eq. (19) and Eq. (20) into lower bound on $\frac{1}{2}\|\mathbf{p}_0\|^2$ we get

$$\begin{aligned} \frac{1}{2}\|\mathbf{p}_0\|^2 &\geq \inf_{\mathbf{q} \in A_\alpha} \log \pi(\mathbf{q}) - \sup_{\mathbf{q} \in B} \log \pi(\mathbf{q}) \\ &\geq \log \lambda - \frac{\alpha^2 d}{2\sigma^2} - \log 2 - \log \lambda + \frac{b^2 d}{2\sigma^2} \\ &= \frac{(b^2 - \alpha^2)d}{2\sigma^2} - \log 2 \\ &\stackrel{(ii)}{>} \frac{(b^2 - \alpha^2)d}{4\sigma^2}, \end{aligned} \quad (21)$$

where (ii) follows from the fact that $b \geq \sqrt{\alpha^2 + 2\sigma^2} > \sqrt{\alpha^2 + (4 \log 2/d)\sigma^2}$ whenever $d \geq 2$. Therefore, we have that $\mathcal{E}(b, d, \alpha) \subseteq \mathcal{E}_1 \subset \mathcal{E}_2$.

Step 2: We now use a Chi-squared tail probability bound on $\mathbb{P}(\mathcal{E}_2)$ to obtain the desired result. Using the fact that $\|\mathbf{p}_0\|^2 \sim \chi_d^2$ when $\mathbf{p}_0 \sim \mathcal{N}(\mathbf{0}, \mathbf{I})$, the Chi-squared tail probability bound yields

$$\begin{aligned} \mathbb{P}(\mathcal{E}(b, d, \alpha)) &< \mathbb{P}(\mathcal{E}_2) = \mathbb{P}\left(\|\mathbf{p}_0\|^2 \geq \frac{(b^2 - \alpha^2)d}{2\sigma^2}\right) \\ &\stackrel{(iii)}{\leq} \exp\left(-\frac{d}{2} \left\{ \frac{b^2 - \alpha^2}{2\sigma^2} - 1 - \log\left(\frac{b^2 - \alpha^2}{2\sigma^2}\right) \right\}\right), \end{aligned}$$

where (iii) uses Ghosh (2021, Eq. 3), which holds whenever $b > \sqrt{\alpha^2 + 2\sigma^2/d}$. This gives us the desired result. \blacksquare

6.2 Proof of Lemma 3.1

For $z_t = \Phi_t^+(z_0)$ we have that

$$\begin{aligned}
\frac{d}{dt}H(z_t) &= \left\langle \nabla_z H(z_t), \frac{d}{dt}z_t \right\rangle \\
&= \nabla_z H(z_t)^\top \left(\Omega \nabla_z H(z_t) + \Gamma z_t \right) \\
&= \nabla_z H(z_t)^\top \Omega \nabla_z H(z_t) + \nabla_z H(z_t)^\top \Gamma z_t \\
&\stackrel{(i)}{=} \nabla_z H(z_t)^\top \Gamma z_t \\
&= \gamma \mathbf{p}_t^\top \Sigma^{-1} \mathbf{p}_t,
\end{aligned}$$

where (i) follows from the fact that $\nabla_z H(z_t)^\top \Omega \nabla_z H(z_t) = \mathbf{0}$, and the final equality follows by noting that $\nabla_z H(z_t) = (\nabla U(\mathbf{q}_t), \Sigma^{-1} \mathbf{p}_t)^\top$. A similar argument for $z_t = \Phi_t^-(z_0)$ gives the final result. \blacksquare

6.3 Proof of Proposition 3.1

Let H be the Hamiltonian satisfying the condition that $H(\mathbf{q}, \mathbf{p}) = H(\mathbf{q}, -\mathbf{p})$. Consider the dynamics of Φ_t^- given by Eq. (9b), i.e.,

$$\frac{d}{dt} \mathbf{q}_t = \nabla_{\mathbf{p}} H(\mathbf{q}_t, \mathbf{p}_t) \quad \text{and} \quad \frac{d}{dt} \mathbf{p}_t = -\nabla_{\mathbf{q}} H(\mathbf{q}_t, \mathbf{p}_t) - \gamma \mathbf{p}_t \tag{22}$$

Let $\tilde{z} = \mathbf{F}(z)$ be given by $(\tilde{\mathbf{q}}, \tilde{\mathbf{p}}) = (\mathbf{q}, -\mathbf{p})$, and take $\tilde{t} = -t$. Then,

$$\frac{d}{d\tilde{t}} \tilde{\mathbf{q}}_t = -\frac{d}{dt} \mathbf{q}_t = -\nabla_{\mathbf{p}} H(\mathbf{q}_t, \mathbf{p}_t) = -\nabla_{\tilde{\mathbf{p}}} H(\tilde{\mathbf{q}}_t, \tilde{\mathbf{p}}_t) = \nabla_{\tilde{\mathbf{p}}} H(\tilde{\mathbf{q}}_t, \tilde{\mathbf{p}}_t),$$

where the final equality follows by noting that $\mathbf{p}_t = -\tilde{\mathbf{p}}_t$. Similarly,

$$\frac{d}{d\tilde{t}} \tilde{\mathbf{p}}_t = \frac{d}{dt} \mathbf{p}_t = -\nabla_{\mathbf{q}} H(\mathbf{q}_t, \mathbf{p}_t) - \gamma \mathbf{p}_t = -\nabla_{\tilde{\mathbf{q}}} H(\tilde{\mathbf{q}}_t, \tilde{\mathbf{p}}_t) + \gamma \tilde{\mathbf{p}}_t,$$

which corresponds to the dynamics of Φ_t^+ in Eq. (9b). Therefore, for $(\mathbf{q}_t, \mathbf{p}_t) = \Phi_t^-(\mathbf{q}_0, \mathbf{p}_0)$ we have

$$\Phi_t^+(\mathbf{F}(\mathbf{q}_t, \mathbf{p}_t)) = \Phi_t^+(\tilde{\mathbf{q}}_t, \tilde{\mathbf{p}}_t) = (\mathbf{q}_0, -\mathbf{p}_0) = \mathbf{F} \circ \Phi_{-t}^-(\mathbf{q}_t, \mathbf{p}_t),$$

or, equivalently, $\Phi_t^+ \circ \mathbf{F} = \mathbf{F} \circ \Phi_{-t}^-$. An identical argument also yields $\Phi_t^- \circ \mathbf{F} = \mathbf{F} \circ \Phi_{-t}^+$, and the first claim follows by noting that $\mathbf{F} \circ \mathbf{F} = \text{id}$.

For the second claim, taking $\Psi_T = \Phi_{T/2}^- \circ \Phi_{T/2}^+$, it follows that

$$\begin{aligned}
(\mathbf{F} \circ \Psi_T) \circ (\mathbf{F} \circ \Psi_T) &= \left(\mathbf{F} \circ \Phi_{T/2}^- \circ \Phi_{T/2}^+ \right) \circ \left(\mathbf{F} \circ \Phi_{T/2}^- \circ \Phi_{T/2}^+ \right) \\
&= \mathbf{F} \circ \Phi_{T/2}^- \circ \Phi_{T/2}^+ \circ \underbrace{\mathbf{F} \circ \Phi_{T/2}^- \circ \Phi_{T/2}^+}_{=\Phi_{-T/2}^+ \circ \mathbf{F}} \\
&= \mathbf{F} \circ \Phi_{T/2}^- \circ \underbrace{\Phi_{T/2}^+ \circ \Phi_{-T/2}^+}_{=\text{id}} \circ \mathbf{F} \circ \Phi_{T/2}^+ \\
&= \mathbf{F} \circ \underbrace{\Phi_{T/2}^- \circ \mathbf{F} \circ \Phi_{T/2}^+}_{=\Phi_{-T/2}^+} \\
&= \Phi_{-T/2}^+ \circ \Phi_{T/2}^+ = \text{id},
\end{aligned}$$

and, therefore, $\mathbf{F} \circ \Psi_T$ is an involution.

For the discrete dynamics, consider one step of the conformal leapfrog step in Algorithm 1, i.e.,

$$\Phi_\epsilon^\pm(\mathbf{q}, \mathbf{p}) = \left(\eta^\pm \circ \underbrace{\xi_1 \circ \xi_2 \circ \xi_1}_{=:\xi} \circ \eta^\pm \right)(\mathbf{q}, \mathbf{p}), \quad (23)$$

where

$$\eta^\pm(\mathbf{q}, \mathbf{p}) := (\mathbf{q}, e^{\pm\gamma\epsilon/2}\mathbf{p}), \quad \xi_1(\mathbf{q}, \mathbf{p}) := (\mathbf{q}, \mathbf{p} - \epsilon/2\nabla U(\mathbf{q})), \quad \text{and} \quad \xi_2(\mathbf{q}, \mathbf{p}) := (\mathbf{q} + \epsilon\Sigma^{-1}\mathbf{p}, \mathbf{p}).$$

For $(\tilde{\mathbf{q}}, \tilde{\mathbf{p}}) = (\mathbf{q}, -\mathbf{p})$, observe that

$$(\eta^+ \circ \mathbf{F} \circ \eta^-)(\tilde{\mathbf{q}}, \tilde{\mathbf{p}}) = \eta^+(\mathbf{q}, -e^{-\gamma\epsilon/2}\mathbf{p}) = (\mathbf{q}, -\mathbf{p}),$$

which implies that $\eta^+ \circ \mathbf{F} \circ \eta^- = \mathbf{F}$. Furthermore, the by noting that the usual leapfrog step $\mathbf{F} \circ \xi$ is an involution, this implies that

$$\begin{aligned} \Phi_\epsilon^- \circ \mathbf{F} \circ \Phi_\epsilon^+ &= \eta^- \circ \xi \circ \underbrace{\eta^- \circ \mathbf{F} \circ \eta^+}_{=\mathbf{F}} \circ \xi \circ \eta^+ \\ &= \eta^- \circ \underbrace{\xi \circ \mathbf{F} \circ \xi}_{=\mathbf{F}} \circ \eta^+ \\ &= \eta^- \circ \mathbf{F} \circ \eta^+ \\ &= \mathbf{F}. \end{aligned}$$

where, the second equality follows from the fact that $\mathbf{F} \circ \xi = \xi \circ \mathbf{F}$ for the usual leapfrog step. A repeated application of the result above yields

$$\Phi_{\epsilon,L}^+ \circ \mathbf{F} \circ \Phi_{\epsilon,L}^- = (\Phi_\epsilon^+)^L \circ \mathbf{F} \circ (\Phi_\epsilon^-)^L = \mathbf{F},$$

and, therefore, $\mathbf{F} \circ \Psi_{\epsilon,L} \circ \mathbf{F} \circ \Psi_{\epsilon,L} = \text{id}$, which is the desired result. \blacksquare

6.4 Proof of Proposition 3.2

The preservation of symplectic structure and, therefore, volume for the continuous time dynamics is a simple consequence of McLachlan and Perlmutter (2001, Proposition 1). See also França et al. (2020). In particular, for the symplectic 2-form

$$\omega_0 = d\mathbf{q}_0 \wedge d\mathbf{p}_0 = \sum_{i=1}^d dq_{0,i} \wedge dp_{0,i}, \quad (24)$$

the symplectic 2-form at time t along the flow φ_t is given by the pullback $\omega_t := (\varphi_t)^*\omega_0 = d\mathbf{q}_t \wedge d\mathbf{p}_t$. From McLachlan and Perlmutter (2001, Proposition 1), it follows that

$$(\Phi_t^+)^*\omega_0 = e^{+\gamma t}\omega_0, \quad \text{and} \quad (\Phi_t^-)^*\omega_0 = e^{-\gamma t}\omega_0.$$

Therefore, for the RAHMC dynamics we have

$$\omega_t = \begin{cases} e^{+\gamma t}\omega_0 & \text{for } 0 \leq t \leq T/2 \\ e^{-\gamma(t-T/2)}\omega_{T/2} = e^{\gamma(T-t)}\omega_0 & \text{for } T/2 \leq t \leq T, \end{cases} \quad (25)$$

and, in particular, at time $t = T$ we have $\omega_T = \omega_0$. Furthermore, since the volume form in the extended phase-space \mathbb{R}^{2d} is the exterior product of the symplectic 2-form, i.e., $\text{vol} := \omega^{\wedge d}$, from Arnold (2013, Chapter 8.38 B, pg. 206), it follows that

$$\text{vol}_t = \begin{cases} e^{+d\gamma t} \text{vol}_0 & \text{for } 0 \leq t \leq T/2 \\ e^{-d\gamma(T-t)} \text{vol}_0 & \text{for } T/2 \leq t \leq T, \end{cases} \quad (26)$$

and $\text{vol}_T = \text{vol}_0$, implying that volume is also conserved in the phase-space at time $t = T$ for the RAHMC dynamics.

For the discrete dynamics in Eq. (23), the determinant of Jacobian for the leapfrog step is $\det(\mathbf{D}\xi) = 1$. It is easy to verify that $\det(\mathbf{D}\eta^\pm) = \exp(\pm\gamma\epsilon/2)$. By the Jacobian chain rule,

$$\det(\mathbf{D}\Phi_\epsilon^\pm) = \det(\mathbf{D}(\eta^\pm \circ \xi \circ \eta^\pm)) = \det(\mathbf{D}\eta^\pm) \det(\mathbf{D}\xi) \det(\mathbf{D}\eta^\pm) = \exp(\pm\gamma\epsilon).$$

Therefore, for $\Psi_{\epsilon,L}$ it follows that

$$\det(\mathbf{D}\Psi_{\epsilon,L}) = \det(\mathbf{D}(\Phi_{\epsilon,L}^- \circ \Phi_{\epsilon,L}^+)) = e^{-L\gamma\epsilon} e^{+L\gamma\epsilon} = 1,$$

which implies that volume is also conserved in the phase-space for the transition $z \mapsto \Psi_{\epsilon,L}(z)$. ■

6.5 Proof of Proposition 3.3

For simplicity let $L = \lfloor T/\epsilon \rfloor$, and let X_{Φ^+} be the Lie derivative operator associated with the dynamics of Eq. (9a), Φ_t^+ , given by

$$X_{\Phi^+} = \Sigma^{-1} \mathbf{p} \frac{\partial}{\partial \mathbf{q}} - (\nabla U(\mathbf{q}) - \gamma \mathbf{p}) \frac{\partial}{\partial \mathbf{p}}.$$

We refer the reader to (Hairer et al., 2006, Chapter III, Section 5) for a detailed treatment of Lie derivatives and their properties. The Lie derivative operator X_{Φ^+} is a first-order differential operator, and, in particular, from Hairer et al. (2006, Chapter III, Eq. 3.5) X_{Φ^+} is the generator of the *exact flow* of Φ^+ via the identity

$$\Phi_t^+(z) = \exp(tX_{\Phi^+}) \text{id}(z).$$

Consider the symmetric (Strang) splitting of X_{Φ^+} given by

$$X_{\Phi^+} = \frac{1}{2}A + \frac{1}{2}B + C + \frac{1}{2}B + \frac{1}{2}A.$$

where

$$A := \gamma \mathbf{p} \frac{\partial}{\partial \mathbf{p}}, \quad B := -\nabla U(\mathbf{q}) \frac{\partial}{\partial \mathbf{p}}, \quad \text{and} \quad C := \Sigma^{-1} \mathbf{p} \frac{\partial}{\partial \mathbf{q}}.$$

For $\epsilon \approx dt$, one step of the conformal leapfrog algorithm for Φ_ϵ^+ as given in Eq. (11) is equivalently written as

$$\Phi_\epsilon^+ = \underbrace{\exp\left(\frac{\epsilon}{2}A\right)}_{=\xi_{\epsilon/2}^\Gamma} \circ \underbrace{\exp\left(\frac{\epsilon}{2}B\right) \circ \exp(\epsilon C) \circ \exp\left(\frac{\epsilon}{2}B\right)}_{=\Phi_\epsilon^H} \circ \underbrace{\exp\left(\frac{\epsilon}{2}A\right)}_{=\xi_{\epsilon/2}^\Gamma} \circ \text{id}.$$

Using the Baker-Campbell-Hausdorff formula, it follows that

$$\begin{aligned}\Phi_\epsilon^+ &\stackrel{(i)}{=} \exp\left(\frac{\epsilon}{2}A\right) \circ \exp\left(\epsilon(B+C) + O(\epsilon^3)\right) \circ \exp\left(\frac{\epsilon}{2}A\right) \circ \text{id} \\ &\stackrel{(ii)}{=} \exp\left(\epsilon(A+B+C) + O(\epsilon^3)\right) \circ \text{id} \\ &= \exp\left(\epsilon X_{\Phi^+} + O(\epsilon^3)\right) \circ \text{id}\end{aligned}$$

where (i) and (ii) follow from (Hairer et al., 2006, Chapter IX, Eq. 4.4), and the final equality follows from the fact that $X_{\Phi^+} = A + B + C$. Mutatis mutandis, an analogous argument for the flow Φ^- yields

$$X_{\Phi^-} := \Sigma^{-1}\mathbf{p} \frac{\partial}{\partial \mathbf{q}} - \left(\nabla U(\mathbf{q}) + \gamma \mathbf{p}\right) \frac{\partial}{\partial \mathbf{p}}, \quad \text{and} \quad \Phi_\epsilon^- = \exp\left(\epsilon X_{\Phi^-} + O(\epsilon^3)\right) \circ \text{id}.$$

Therefore, for the transition $z \mapsto \Psi_{\epsilon,L}(z)$, it follows that

$$\begin{aligned}\Psi_{\epsilon,L} &= \Phi_{\epsilon,L/2}^- \circ \Phi_{\epsilon,L/2}^+ \\ &= (\Phi_\epsilon^-)^{L/2} \circ (\Phi_\epsilon^+)^{L/2} \\ &\stackrel{(iii)}{=} \exp\left(\frac{L\epsilon}{2}X_{\Phi^+} + O(L\epsilon^3)\right) \circ \exp\left(\frac{L\epsilon}{2}X_{\Phi^-} + O(L\epsilon^3)\right) \circ \text{id} \\ &\stackrel{(iv)}{=} \exp\left(\frac{T}{2}X_{\Phi^+} + O(\epsilon^2)\right) \circ \exp\left(\frac{T}{2}X_{\Phi^-} + O(\epsilon^2)\right) \circ \text{id} \\ &\stackrel{(v)}{=} \exp\left(\frac{T}{2}X_{\Phi^+} + O(\epsilon^2)\right) \circ \exp\left(\frac{T}{2}X_{\Phi^-}\right) \circ \text{id} + O(\epsilon^2) \\ &\stackrel{(vi)}{=} \exp\left(\frac{T}{2}X_{\Phi^+}\right) \circ \exp\left(\frac{T}{2}X_{\Phi^-}\right) \circ \text{id} + O(\epsilon^2) \\ &= \Phi_{T/2}^- \circ \Phi_{T/2}^+ + O(\epsilon^2) \\ &= \Psi_T + O(\epsilon^2)\end{aligned}$$

where (iii) follows from Gröbner's lemma (Hairer et al., 2006, Chapter III, Lemma 5.1) and the fact that $\exp(M)^L = \exp(LM)$, (iv) uses the substitution $T = L\epsilon$, and (v, vi) follow from the fact that $\exp(\epsilon^2 M) \circ f = (\text{id} + O(\epsilon^2 M)) \circ f = f + O(\epsilon^2)$. Therefore, the error in the approximation of Ψ_T by $\Psi_{\epsilon,L}$ is

$$\|\Psi_{\epsilon,L}(z) - \Psi_T(z)\| = O(\epsilon^2), \quad \text{for } L = O(1/\epsilon) \text{ steps.}$$

Since $U(\mathbf{q})$ is ℓ -Lipschitz, it follows that $|H(z) - H(z')| \leq C\|z - z'\|$ where $C = \max\{\ell, \|\Sigma^{-1}\|\}$, and, we have that

$$|H(\Psi_{\epsilon,L}(z)) - H(\Psi_{\epsilon,L}(z'))| \leq O(\epsilon^2).$$

■

6.6 Proof of Proposition 3.4

To ease the notation and to make the presentation of the proof consistent with the literature in dynamical systems and control theory (e.g., Sastry, 2013, Khalil, 2002), we will make use of several notational conventions. For $z_t, \mathbf{q}_t, \mathbf{p}_t$, wherever the dependence on time is clear from context, we will drop the subscript t and express them as $z, \mathbf{p}, \mathbf{q}$, and the (autonomous) conformal Hamiltonian system from Eq. (9b) by

$$\begin{pmatrix} \dot{\mathbf{q}} \\ \dot{\mathbf{p}} \end{pmatrix} = \begin{pmatrix} \Sigma^{-1}\mathbf{p} \\ -\nabla U(\mathbf{q}) - \gamma \mathbf{p} \end{pmatrix} =: f(\mathbf{q}, \mathbf{p}), \quad (27)$$

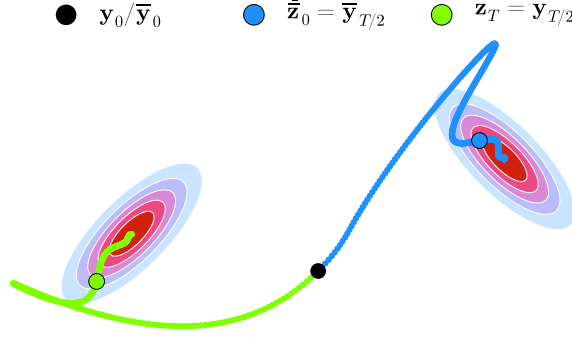


Figure 10: The figure illustrates the key ingredients of the proof in the state-space for $\mathbf{q} \in \mathbb{R}^d$. For $\mathbf{z}_0 \in \mathbb{R}^{2d}$ (green point), we take $\mathbf{y}_0 := \Phi_{T/2}^+(\mathbf{z}_0)$ and $\bar{\mathbf{y}}_0 := \mathbf{F}(\mathbf{y}_0)$. Since $\mathbf{F}(\mathbf{q}, \mathbf{p}) = (\mathbf{q}, -\mathbf{p})$, the projections of \mathbf{y}_0 and $\bar{\mathbf{y}}_0$ on the state-space \mathbb{R}^d are the same point, shown in black. From Proposition 3.1, it follows that $\mathbf{y}_{T/2} = \Phi_{T/2}^-(\mathbf{y}_0) = \mathbf{z}_T$ and $\bar{\mathbf{y}}_{T/2} = \Phi_{T/2}^-(\bar{\mathbf{y}}_0) = \mathbf{z}_0$ (blue point). By the invariance of the Hamiltonian under \mathbf{F} , $H(\bar{\mathbf{z}}_0) = H(\mathbf{z}_0)$. We show that $H(\mathbf{y}_t)$ and $H(\bar{\mathbf{y}}_t)$ decay exponentially along the green and blue trajectories, respectively. The proof, then, follows by combining these results. We also note that although the black point is the same for \mathbf{y}_0 and $\bar{\mathbf{y}}_0$ in the state-space; in the phase-space, the momenta are flipped, therefore \mathbf{y}_0 and $\bar{\mathbf{y}}_0$ are reflections about the $\{(\mathbf{q}, \mathbf{0}) : \mathbf{q} \in \mathbb{R}^d\}$ subspace.

where $\gamma > 0$, $(\dot{\mathbf{q}}, \dot{\mathbf{p}}) := (\frac{d}{dt}\mathbf{q}_t, \frac{d}{dt}\mathbf{p}_t)$, and $f(\mathbf{q}, \mathbf{p}) : \mathbb{R}^{2d} \rightarrow \mathbb{R}^{2d}$ is the vector field describing the dynamics of the conformal Hamiltonian system. For a function $G : \mathbb{R}^{2d} \rightarrow \mathbb{R}$, the time derivative of G along the trajectories $(\mathbf{q}_t, \mathbf{p}_t) = \Phi_t^-(\mathbf{q}, \mathbf{p})$ of Eq. (27) is given by $\dot{G}(t) := \nabla G(t)^\top f(\mathbf{q}, \mathbf{p})$.

Let $\mathbf{z}_0 \in \mathbb{R}^{2d}$ be the initial state at $t = 0$ and let $\mathbf{z}_T = \Psi_T(\mathbf{z}_0)$ be the final proposed state by RAHMC at time $t = T$. We are going to translate the time parameter t to consider $\mathbf{y}_0 = \Phi_{T/2}^+(\mathbf{z}_0)$ as the intermediate state of the RAHMC trajectory at time $t = T/2$ and let $\bar{\mathbf{y}}_0 = \mathbf{F}(\mathbf{y}_0)$ be the state obtained by flipping the momentum of \mathbf{y}_0 . We also $(\mathbf{u}, \mathbf{v}) := \mathbf{y}$ to denote the position and momentum variables for the state \mathbf{y} , so as to distinguish them from (\mathbf{q}, \mathbf{p}) which are used for \mathbf{z} . From Proposition 3.1, it follows that $\mathbf{z}_T = \Phi_{T/2}^-(\mathbf{y}_0)$ and $\bar{\mathbf{z}}_0 = \Phi_{T/2}^-(\bar{\mathbf{y}}_0)$.

With this background, the outline of the proof is as follows. See Figure 10 for an illustration.

1. From assumptions on U , we establish that the trajectories $\Phi_t^-(\mathbf{y}_0)$ and $\Phi_t^-(\bar{\mathbf{y}}_0)$ are well-defined and unique for all time $t \geq 0$, which pass through $\bar{\mathbf{z}}_0$ and \mathbf{z}_T . Their limit points¹, $\ell(\mathbf{y}_0) = \lim_{t \rightarrow \infty} \Phi_t^-(\mathbf{y}_0)$ and $\ell(\bar{\mathbf{y}}_0) = \lim_{t \rightarrow \infty} \Phi_t^-(\bar{\mathbf{y}}_0)$, are unique points in \mathcal{S} , which are non-degenerate and isolated critical points of $f(\mathbf{q}, \mathbf{p})$.
2. Using standard Lyapunov analysis, we show that the Hamiltonian $H(t)$ is exponentially decaying along the trajectory $\Phi_t^-(\mathbf{y}_0)$, i.e.,

$$(H(t) - H^*) \leq (H(0) - H^*)e^{-\lambda t}, \quad (28)$$

where $H^* := H(\ell(\mathbf{y}_0))$ and $\lambda > 0$ is a constant. An identical result holds for the trajectory $\Phi_t^-(\bar{\mathbf{y}}_0)$.

3. Combining steps 1 and 2, we obtain the final bound on $|H(\mathbf{z}_0) - H(\mathbf{z}_T)|$.

Step 1. We begin by noting that the critical points of $f(\mathbf{q}, \mathbf{p})$ are the points in \mathcal{S} , i.e.,

$$\text{crit } f := \left\{ (\mathbf{q}, \mathbf{p}) \in \mathbb{R}^{2d} : f(\mathbf{q}, \mathbf{p}) = \mathbf{0}_{2d} \right\} = \left\{ (\mathbf{q}^*, \mathbf{0}) \in \mathbb{R}^{2d} : \nabla U(\mathbf{q}^*) = \mathbf{0}_d \right\}.$$

¹Technically, their ω -limit points (Sastry, 2013, Definition 5.18)

Moreover, by the assumption that U is a Morse function, it follows that the Hessian $\nabla^2 U(\mathbf{q}^*)$ is non-degenerate for all critical points \mathbf{q}^* (Nicolaeescu, 2011, Definition 1.7), and from the Morse lemma (Milnor, 1963, Lemma 2.2 and Corollary 2.3), it also follows that the set of critical points $(\mathbf{q}^*, \mathbf{0}) \in \mathcal{S}$ are isolated.

From assumption (A2), ∇U is Lipschitz gradients, and we have

$$\begin{aligned} \|f(\mathbf{q}, \mathbf{p}) - f(\mathbf{q}', \mathbf{p}')\| &\stackrel{(i)}{\leq} \sqrt{(1 + \gamma^2)\|\mathbf{p} - \mathbf{p}'\|^2 + \|\nabla U(\mathbf{q}) - \nabla U(\mathbf{q}')\|^2} \\ &\stackrel{(ii)}{\leq} \sqrt{(1 + \gamma^2)\|\mathbf{p} - \mathbf{p}'\|^2 + \beta^2\|\mathbf{q} - \mathbf{q}'\|^2} \\ &\leq L_f \|(\mathbf{q}, \mathbf{p}) - (\mathbf{q}', \mathbf{p}')\|, \end{aligned}$$

where (i) follows from the triangle inequality, and (ii) invokes assumption (A1), where the constant $L_f = \max\{\beta, 1 + \gamma\}$. It follows that vector field, $f(\mathbf{q}, \mathbf{p})$, is Lipschitz continuous. Therefore, by the Picard-Lindelöf theorem, for any initial condition $\mathbf{y}_0 \in \mathbb{R}^{2d}$, there exists a unique solution $\Phi_t^-(\mathbf{y}_0)$ to Eq. (27) for all $t \geq 0$ (Sastry, 2013, Theorem3.22).

For the points $\mathbf{y}_0, \bar{\mathbf{y}}_0 \in \mathbb{R}^{2d}$, let $a := H(\mathbf{y}_0) = H(\bar{\mathbf{y}}_0)$, $(\mathbf{u}_t, \mathbf{v}_t) := \Phi_t^-(\mathbf{y}_0)$ be the trajectory \mathbf{y}_t along Eq. (27), and $H(t) = H(\mathbf{u}_t, \mathbf{v}_t)$. From Lemma 3.1, it follows that $\dot{H}(t) = -\gamma \mathbf{v}_t^\top \Sigma^{-1} \mathbf{v}_t \leq 0$, i.e., $H(t)$ is non-increasing along the trajectory $\Phi_t^-(\mathbf{y}_0)$. In particular, for the sublevel set of the Hamiltonian, given by $\widehat{H}(a) := \{(\mathbf{q}, \mathbf{p}) \in \mathbb{R}^{2d} : H(\mathbf{q}, \mathbf{p}) \leq a\}$, it follows that $(\mathbf{u}_t, \mathbf{v}_t) \in \widehat{H}(a)$ for all $t \geq 0$. Furthermore, since U is coercive, i.e., $\lim_{\|\mathbf{u}\| \rightarrow \infty} U(\mathbf{u}) = \infty$, it follows that the sublevel set $\widehat{H}(a)$ is bounded and compact. Applying LaSalle's invariance principle (Sastry, 2013, Section 5.4), it follows that $\Phi_t^-(\mathbf{y}_0)$ approaches \mathcal{S} as $t \rightarrow \infty$. An application of Attouch et al. (2000, Theorem 4.1) further guarantees that $\lim_{t \rightarrow \infty} \Phi_t^-(\mathbf{y}_0) = \ell(\mathbf{y}_0) \in \mathcal{S}$. An identical result holds for the trajectory $\Phi_t^-(\bar{\mathbf{y}}_0)$.

Lastly, for $\mathbf{z}^* \in \mathcal{S}$, let $\mathcal{W}(\mathbf{z}^*)$ be the set of initial conditions \mathbf{z} such that $\Phi_t^-(\mathbf{z})$ converges to \mathbf{z}^* , i.e.,

$$\mathcal{W}(\mathbf{z}^*) := \left\{ \mathbf{z} \in \mathbb{R}^{2d} : \lim_{t \rightarrow \infty} \Phi_t^-(\mathbf{z}) = \mathbf{z}^* \right\}.$$

The set $\mathcal{W}(\mathbf{z}^*)$ is called the domain of attraction/stable manifold of \mathbf{z}^* . From Sastry (2013, Proposition 5.44), it follows that $\mathcal{W}(\mathbf{z}^*)$ is an open, invariant set, and, from the previous discussion, it follows that $\mathcal{W}(\ell(\mathbf{y}_0)), \mathcal{W}(\ell(\bar{\mathbf{y}}_0)) \subset \widehat{H}(a)$ are both open, invariant sets. Therefore, if $\bar{\mathbf{z}}_0 \in \mathcal{W}(\mathbf{z}^*)$, it follows that $\mathbf{y}_0 = \Phi_{-t}^-(\bar{\mathbf{z}}_0) \in \mathcal{W}(\mathbf{z}^*)$.

To summarize, for $\mathbf{y}_0, \bar{\mathbf{y}}_0 \in \mathbb{R}^{2d}$ we have that $\ell(\mathbf{y}_0) = \lim_{t \rightarrow \infty} \Phi_t^-(\mathbf{y}_0)$ and $\ell(\bar{\mathbf{y}}_0) = \lim_{t \rightarrow \infty} \Phi_t^-(\bar{\mathbf{y}}_0)$ are non-degenerate, and isolated critical points in \mathcal{S} .

Step 2. We now show that the Hamiltonian $H(t)$ decays exponentially along the trajectory $\Phi_t^-(\mathbf{y}_0)$. We are interested in obtaining an inequality of the type $\dot{H}(t) \leq -\lambda H(t)$ for some $\lambda > 0$. The issue with working with the Hamiltonian, $H(t)$, directly is that $\dot{H}(t) \leq -\gamma \mathbf{p}_t^\top \Sigma^{-1} \mathbf{p}_t$, suggesting that $H(t)$ may suddenly stop decreasing when $\mathbf{p}_t = \mathbf{0}$. This is, however, not the case since the dynamics of Eq. (9) and Eq. (27) nudge the momentum away from these singularities. Therefore, in order to establish the exponential decay of $H(t)$, we will work with a modified Lyapunov function, $V(t)$. This technique is standard in the literature on dynamical systems and control theory, and, more recently in optimization. We refer the reader to Bégout et al. (2015), Polyak and Shcherbakov (2018), Maddison et al. (2018), Muehlebach and Jordan (2021), Viorel et al. (2020), where similar techniques are used.

In particular, for a small $h > 0$ we employ the Lyapunov function

$$V(t) := V(\mathbf{q}, \mathbf{p}) = \underbrace{\frac{1}{2} \mathbf{p}^\top \Sigma^{-1} \mathbf{p} + U(\mathbf{q}) - U(\mathbf{q}^*)}_{=H(\mathbf{q}, \mathbf{p})} + h \cdot \underbrace{\mathbf{p}^\top \Sigma^{-1} \nabla U(\mathbf{q})}_{=: \eta(\mathbf{q}, \mathbf{p})}, \quad (29)$$

which is similar to the Lyapunov function in Polyak and Shcherbakov (2018, Eq. 6). The time derivative of $V(t)$ along $f(\mathbf{q}, \mathbf{p})$ is given by

$$\begin{aligned}
\dot{V}(t) &= \nabla V(t)^\top f(\mathbf{q}, \mathbf{p}) \\
&= \dot{H}(t) + h \cdot \left(\nabla \eta(\mathbf{q}_t, \mathbf{p}_t)^\top f(\mathbf{q}, \mathbf{p}) \right) \\
&= -\gamma \mathbf{p}^\top \Sigma^{-1} \mathbf{p} + h \cdot \left(\mathbf{p}^\top (\Sigma^{-1} \nabla^2 U(\mathbf{q}) \Sigma^{-1}) \mathbf{p} - \gamma \cdot \mathbf{p}^\top \Sigma^{-1} \nabla U(\mathbf{q}) - \nabla U(\mathbf{q})^\top \Sigma^{-1} \nabla U(\mathbf{q}) \right) \\
&= -\hat{\mathbf{p}}^\top (\gamma \mathbf{I} - h \mathbf{A}) \hat{\mathbf{p}} - h \gamma \hat{\mathbf{p}}^\top \Sigma^{-1/2} \nabla U(\mathbf{q}) - h \nabla U(\mathbf{q})^\top \Sigma^{-1} \nabla U(\mathbf{q}), \tag{30}
\end{aligned}$$

where $\hat{\mathbf{p}} := \Sigma^{-1/2} \mathbf{p}$ and $\mathbf{A} := \Sigma^{-1/2} \cdot \nabla^2 U(\mathbf{q}) \cdot \Sigma^{-1/2}$. By Young's inequality, the second term can be bounded by

$$\hat{\mathbf{p}}^\top \Sigma^{-1/2} \nabla U(\mathbf{q}) = \hat{\mathbf{p}}^\top \left(\Sigma^{-1/2} \nabla U(\mathbf{q}) \right) \geq -\frac{1}{2} \hat{\mathbf{p}}^\top \hat{\mathbf{p}} - \frac{1}{2} \nabla U(\mathbf{q})^\top \Sigma^{-1} \nabla U(\mathbf{q}). \tag{31}$$

Substituting this back into Eq. (30), we obtain

$$\dot{V}(t) \leq -\frac{1}{2} \hat{\mathbf{p}}^\top \mathbf{B} \hat{\mathbf{p}} - h \nabla U(\mathbf{q})^\top \Sigma^{-1} \nabla U(\mathbf{q}), \tag{32}$$

where $\mathbf{B} := (\gamma - \frac{h}{2}) \mathbf{I} - h \mathbf{A}$. Using $\sigma_{\max}(\mathbf{X}) = \sigma_1(\mathbf{X}) \geq \sigma_2(\mathbf{X}) \geq \dots \geq \sigma_{2d}(\mathbf{X}) = \sigma_{\min}(\mathbf{X})$ to denote the eigenvalues of a matrix \mathbf{X} , the first term in Eq. (32) is bounded by

$$\hat{\mathbf{p}}^\top \mathbf{B} \hat{\mathbf{p}} \geq \sigma_{\min}(\mathbf{B}) \|\hat{\mathbf{p}}\|^2 = \sigma_{\min} \left(\left(\gamma - \frac{h}{2} \right) \mathbf{I} - h \mathbf{A} \right) \|\hat{\mathbf{p}}\|^2 \geq \left(\gamma - \frac{h}{2} - h \frac{\varpi}{\sigma_{\min}(\Sigma)} \right) \|\hat{\mathbf{p}}\|^2,$$

where the last inequality follows from the fact that $\sigma_{\max}(\mathbf{A}) \leq \sigma_{\max}(\Sigma^{-1}) \sigma_{\max}(\nabla^2 U(\mathbf{q})) \leq \varpi / \sigma_{\min}(\Sigma)$. Therefore, $\hat{\mathbf{p}}^\top \mathbf{B} \hat{\mathbf{p}} \geq 0$ whenever $h \in (0, h_0)$ for

$$h_0 := \frac{2\gamma \sigma_{\min}(\Sigma)}{2\varpi + \sigma_{\min}(\Sigma)}.$$

For simplicity, we will take $h = h_0/2$, which implies that $\hat{\mathbf{p}}^\top \mathbf{B} \hat{\mathbf{p}} \geq \gamma \|\hat{\mathbf{p}}\|^2/2$. Similarly, the second term in Eq. (32) is bounded by

$$\nabla U(\mathbf{q})^\top \Sigma^{-1} \nabla U(\mathbf{q}) \geq \frac{1}{\sigma_{\max}(\Sigma)} \|\nabla U(\mathbf{q})\|^2 \geq \frac{\mu}{\sigma_{\max}(\Sigma)} (U(\mathbf{q}) - U(\mathbf{q}^*)),$$

where the last inequality follows from the fact that U satisfies the Polyak-Łojasiewicz condition. Plugging this into Eq. (32), we obtain

$$\dot{V}(t) \leq -\frac{\gamma}{2} \|\hat{\mathbf{p}}\|^2 - \frac{h_0 \mu}{2\sigma_{\max}(\Sigma)} (U(\mathbf{q}) - U(\mathbf{q}^*)) \leq -\lambda_1 V(t), \tag{33}$$

for

$$\lambda_1 := \min \left\{ \frac{\gamma}{2}, \frac{h_0 \mu}{2\sigma_{\max}(\Sigma)} \right\}.$$

Using the Grönwall-Bellman lemma (Sastry, 2013, Proposition 3.21), it follows that

$$V(t) \leq V(0) e^{-\lambda_1 t}. \tag{34}$$

Similarly, taking $W(t) = U(\mathbf{q}) - U(\mathbf{q}^*)$, it follows that

$$\begin{aligned}
\dot{W}(t) &= \nabla W(\mathbf{q}, \mathbf{p})^\top f(\mathbf{q}, \mathbf{p}) \\
&= \mathbf{p}^\top \Sigma^{-1} \nabla U(\mathbf{q}) \\
&\stackrel{\text{(iii)}}{=} \frac{1}{h} \cdot \left(V(t) - \frac{1}{2} \|\widehat{\mathbf{p}}\|^2 - W(t) \right) \\
&\stackrel{\text{(iv)}}{\leq} -\frac{1}{h} W(t) + \frac{1}{h} V(0) e^{-\lambda_1 t},
\end{aligned} \tag{35}$$

where (iii) follows from the definition of $V(t)$ in Eq. (29), and (iv) follows from Eq. (34) and by noting that $\|\widehat{\mathbf{p}}\|^2 \geq 0$. Therefore, by the method of variation of parameters it follows that $W(t)$ decays exponentially as well with a rate $\lambda_2 = \min \{ \lambda_1, 1/h \}$.

Lastly, for $X(t) = \frac{1}{2} \mathbf{p}^\top \Sigma^{-1} \mathbf{p}$, it follows that

$$\begin{aligned}
\dot{X}(t) &= \nabla X(\mathbf{q}, \mathbf{p})^\top f(\mathbf{q}, \mathbf{p}) \\
&= -\gamma \mathbf{p}^\top \Sigma^{-1} \mathbf{p} - \mathbf{p}^\top \Sigma^{-1} \nabla U(\mathbf{q}) \\
&\stackrel{\text{(v)}}{\leq} -\gamma \widehat{\mathbf{p}}^\top \widehat{\mathbf{p}} - \frac{1}{2} \widehat{\mathbf{p}}^\top \widehat{\mathbf{p}} - \frac{1}{2} \nabla U(\mathbf{q}) \Sigma^{-1} \nabla U(\mathbf{q}) \\
&\stackrel{\text{(vi)}}{\leq} -\left(\gamma + \frac{1}{2} \right) \|\widehat{\mathbf{p}}\|^2 \\
&= -(2\gamma + 1) X(t)
\end{aligned}$$

where (v) follows from Young's inequality in Eq. (31) and (vi) follows from the the fact that $\nabla U(\mathbf{q}) \Sigma^{-1} \nabla U(\mathbf{q}) \geq 0$. Therefore, $X(t)$ decays exponentially as well with a rate $\lambda_3 = 2\gamma + 1$, i.e., $X(t) = X(0) e^{-\lambda_3 t}$. Combining the results we get

$$\begin{aligned}
H(t) - H^* &= X(t) + W(t) \\
&\leq X(0) e^{-\lambda_3 t} + W(0) e^{-\lambda_2 t} \\
&\leq (X(0) + W(0)) e^{-\min \{ \lambda_2, \lambda_3 \} t} \\
&= (H(0) - H^*) e^{-\lambda t},
\end{aligned} \tag{36}$$

where

$$\lambda = \min \left\{ \frac{\gamma}{2}, \frac{\gamma \mu \sigma_{\min}(\Sigma)}{(2\varpi + \sigma_{\min}(\Sigma)) \sigma_{\max}(\Sigma)}, \frac{2\varpi + \sigma_{\min}(\Sigma)}{2\gamma \sigma_{\min}(\Sigma)} \right\}. \tag{37}$$

Step 3. Let $\mathbf{z}_0 \in \mathbb{R}^{2d}$ and $\mathbf{z}_T = \Psi_T(\mathbf{z}_0)$, and as described earlier let $\mathbf{y}_0 = \Phi_{T/2}^+(\mathbf{z}_0)$ and $\bar{\mathbf{y}}_0 = \mathbf{F}(\mathbf{y}_0)$. Furthermore, let $\mathbf{y}^* = \ell(\mathbf{y}_0)$ and $\bar{\mathbf{y}}^* = \ell(\bar{\mathbf{y}}_0)$ be the critical points that the trajectories starting from \mathbf{y}_0 and $\bar{\mathbf{y}}_0$ at time $t = 0$ converge to along Φ_t^- . From the results in Step 2, it follows that

$$\begin{aligned}
|H(\mathbf{z}_0) - H(\mathbf{z}_T)| &\stackrel{\text{(vii)}}{=} \left| H(\bar{\mathbf{z}}_0) - H(\bar{\mathbf{y}}^*) + H(\bar{\mathbf{y}}^*) - H(\mathbf{y}^*) + H(\mathbf{y}^*) - H(\mathbf{z}_T) \right| \\
&\stackrel{\text{(viii)}}{=} \left| H(\bar{\mathbf{y}}_{T/2}) - H(\bar{\mathbf{y}}^*) \right| + \left| H(\bar{\mathbf{y}}^*) - H(\mathbf{y}^*) \right| + \left| H(\mathbf{y}^*) - H(\mathbf{y}_{T/2}) \right|
\end{aligned}$$

$$\begin{aligned} \therefore |H(\mathbf{z}_0) - H(\mathbf{z}_T)| &\stackrel{\text{(ix)}}{\leq} (H(\bar{\mathbf{y}}_0) - H(\bar{\mathbf{y}}^*))e^{-\lambda T/2} + (H(\mathbf{y}_0) - H(\mathbf{y}^*))e^{-\lambda T/2} + |H(\bar{\mathbf{y}}^*) - H(\mathbf{y}^*)| \\ &\stackrel{\text{(x)}}{=} \left(H(\mathbf{z}_{T/2}) - H(\mathbf{y}^*) - H(\bar{\mathbf{y}}^*) \right) e^{-\lambda T/2} + |H(\bar{\mathbf{y}}^*) - H(\mathbf{y}^*)|, \end{aligned}$$

where (vii) uses the fact that $H(\mathbf{z}_0) = H(\bar{\mathbf{z}}_0)$, (viii) uses the fact that $\mathbf{z}_T = \Phi_{T/2}^-(\mathbf{y}_0)$ and $\bar{\mathbf{z}}_0 = \Phi_{T/2}^-(\bar{\mathbf{y}}_0)$, (ix) uses Eq. (36), and (x) uses the fact that $\mathbf{y}_0 = \Phi_{T/2}^+(\mathbf{z}_0)$ and $H(\mathbf{y}_0) = H(\bar{\mathbf{y}}_0)$. Taking the supremum over all $\mathbf{y}^*, \bar{\mathbf{y}}^* \in \mathcal{S}$,

$$|H(\mathbf{z}_0) - H(\mathbf{z}_T)| \leq \sup_{\mathbf{a}, \mathbf{b} \in \mathcal{S}} \left(H(\mathbf{z}_{T/2}) - H(\mathbf{a}) - H(\mathbf{b}) \right) e^{-\lambda T/2} + |H(\mathbf{a}) - H(\mathbf{b})|,$$

which gives us the final result. ■

Acknowledgement

SV and HT would like to thank Xiao-Li Meng and David van Dyk for their insightful comments on the first draft of this manuscript. SV would also like to thank Ann Johnston for helpful discussions and feedback.

References

- M. Agarwal and D. Vats. Globally centered autocovariances in MCMC. *Journal of Computational and Graphical Statistics*, 31(3):629–638, 2022.
- J. Alenlöv, A. Doucet, and F. Lindsten. Pseudo-marginal Hamiltonian Monte Carlo. *Journal of Machine Learning Research*, 22(141):1–45, 2021.
- C. Andrieu, N. De Freitas, A. Doucet, and M. I. Jordan. An introduction to MCMC for machine learning. *Machine Learning*, 50:5–43, 2003.
- V. I. Arnold. *Mathematical Methods of Classical Mechanics*, volume 60. Springer Science & Business Media, 2013.
- H. Attouch, X. Goudou, and P. Redont. The heavy ball with friction method, I. the continuous dynamical system: Global exploration of the local minima of a real-valued function by asymptotic analysis of a dissipative dynamical system. *Communications in Contemporary Mathematics*, 2(01):1–34, 2000.
- A. Banyaga, D. Hurtubise, and D. Ajayi. *Lectures on Morse Homology*. Springer, 2004.
- A. Barp, F.-X. Briol, A. D. Kennedy, and M. Girolami. Geometry and dynamics for Markov chain Monte Carlo. *Annual Review of Statistics and Its Application*, 5:451–471, 2018.
- P. Bégout, J. Bolte, and M. A. Jendoubi. On damped second-order gradient systems. *Journal of Differential Equations*, 259(7):3115–3143, 2015.
- G. Benettin and A. Giorgilli. On the Hamiltonian interpolation of near-to-the identity symplectic mappings with application to symplectic integration algorithms. *Journal of Statistical Physics*, 74:1117–1143, 1994.
- A. Beskos, N. Pillai, G. Roberts, J.-M. Sanz-Serna, and A. Stuart. Optimal tuning of the hybrid Monte Carlo algorithm. *Bernoulli*, 19(5a):1501 – 1534, 2013.

- M. Betancourt. Adiabatic Monte Carlo. *arXiv preprint arXiv:1405.3489*, 2014.
- M. Betancourt. A Conceptual Introduction to Hamiltonian Monte Carlo. *arXiv e-prints*, art. arXiv:1701.02434, Jan. 2017.
- M. Betancourt, S. Byrne, S. Livingstone, and M. Girolami. The geometric foundations of Hamiltonian Monte Carlo. *Bernoulli*, 23(4a):2257–2298, 2017.
- K. Binder, D. W. Heermann, and K. Binder. *Monte Carlo Simulation in Statistical Physics*, volume 8. Springer, 1992.
- J. A. Brofos and R. R. Lederman. Non-canonical Hamiltonian Monte Carlo. *arXiv preprint arXiv:2008.08191*, 2020.
- S. Brooks, A. Gelman, G. Jones, and X.-L. Meng. *Handbook of Markov Chain Monte Carlo*. CRC press, 2011.
- G. Celeux, M. Hurn, and C. P. Robert. Computational and inferential difficulties with mixture posterior distributions. *Journal of the American Statistical Association*, 95(451):957–970, 2000. ISSN 01621459.
- T. Chen, E. Fox, and C. Guestrin. Stochastic gradient Hamiltonian Monte Carlo. In *International conference on machine learning*, pages 1683–1691. Pmlr, 2014.
- M. Cuturi. Sinkhorn distances: Lightspeed computation of optimal transport. *Advances in Neural Information Processing Systems*, 26, 2013.
- S. Duane, A. D. Kennedy, B. J. Pendleton, and D. Roweth. Hybrid Monte Carlo. *Physics Letters B*, 195(2): 216–222, Sept. 1987.
- N. Fournier and A. Guillin. On the rate of convergence in Wasserstein distance of the empirical measure. *Probability Theory and Related Fields*, 162(3-4):707, 2015.
- G. França, J. Sulam, D. P. Robinson, and R. Vidal. Conformal symplectic and relativistic optimization. *Journal of Statistical Mechanics: Theory and Experiment*, 2020(12):124008, 2020.
- A. Gelman, J. B. Carlin, H. S. Stern, and D. B. Rubin. *Bayesian Data Analysis*. Chapman and Hall/CRC, 1995.
- M. Ghosh. Exponential tail bounds for Chi squared random variables. *Journal of Statistical Theory and Practice*, 15(2):1–6, 2021.
- M. Girolami and B. Calderhead. Riemann manifold Langevin and Hamiltonian Monte Carlo methods. *Journal of the Royal Statistical Society: Series B (Statistical Methodology)*, 73(2):123–214, 2011.
- G. Gobbo and B. J. Leimkuhler. Extended Hamiltonian approach to continuous tempering. *Physical Review E*, 91(6):061301, 2015.
- M. Graham and A. Storkey. Continuously tempered Hamiltonian Monte Carlo. In *Conference on Uncertainty in Artificial Intelligence*, 2017.
- E. Hairer, C. Lubich, and G. Wanner. *Geometric Numerical Integration: Structure-Preserving Algorithms for Ordinary Differential Equations*, volume 31. Springer Science & Business Media, 2006.
- W. K. Hastings. Monte Carlo sampling methods using Markov chains and heir applications. *Biometrika*, 57 (1):97–109, 1970.

- M. D. Hoffman and A. Gelman. The No-U-Turn sampler: Adaptively setting path lengths in Hamiltonian Monte Carlo. *Journal of Machine Learning Research*, 15(47):1593–1623, 2014.
- H. Khalil. *Nonlinear Systems*. Pearson Education. Prentice Hall, 2002. ISBN 9780130673893.
- S. C. Kou, Q. Zhou, and W. H. Wong. Equi-energy sampler with applications in statistical inference and statistical mechanics. *The Annals of Statistics*, 34(4):1581 – 1619, 2006.
- J. S. Lamb and J. A. Roberts. Time-reversal symmetry in dynamical systems: A survey. *Physica D: Nonlinear Phenomena*, 112(1-2):1–39, 1998.
- S. Lan, J. Streets, and B. Shahbaba. Wormhole Hamiltonian Monte Carlo. *Proceedings of the AAAI Conference on Artificial Intelligence*, pages 1953–1959, 2014.
- B. Leimkuhler and S. Reich. A Metropolis adjusted Nosé-Hoover thermostat. *ESAIM: Mathematical Modelling and Numerical Analysis*, 43(4):743–755, 2009.
- D. Levy, M. D. Hoffman, and J. Sohl-Dickstein. Generalizing Hamiltonian Monte Carlo with neural networks. In *International Conference on Learning Representations*, 2018.
- Z. Liu and Z. Zhang. Quantum-inspired Hamiltonian Monte Carlo for Bayesian sampling. *ArXiv*, abs/1912.01937, 2019.
- S. Livingstone, M. Betancourt, S. Byrne, and M. Girolami. On the geometric ergodicity of Hamiltonian Monte Carlo. 2019.
- X. Lu, V. Perrone, L. Hasenclever, Y. W. Teh, and S. Vollmer. Relativistic Monte Carlo. In *Artificial Intelligence and Statistics*, pages 1236–1245. Pmlr, 2017.
- R. Luo, J. Wang, Y. Yang, J. Wang, and Z. Zhu. Thermostat-assisted continuously-tempered Hamiltonian Monte Carlo for Bayesian learning. *Advances in Neural Information Processing Systems*, 31, 2018.
- C. J. Maddison, D. Paulin, Y. W. Teh, B. O’Donoghue, and A. Doucet. Hamiltonian descent methods. *arXiv preprint arXiv:1809.05042*, 2018.
- O. Mangoubi, N. S. Pillai, and A. Smith. Does Hamiltonian Monte Carlo mix faster than a random walk on multimodal densities?, 2018.
- R. McLachlan and M. Perlmutter. Conformal Hamiltonian systems. *Journal of Geometry and Physics*, 39(4): 276–300, 2001.
- N. Metropolis, A. W. Rosenbluth, M. N. Rosenbluth, A. H. Teller, and E. Teller. Equation of State Calculations by Fast Computing Machines. *The Journal of Chemical Physics*, 21(6):1087–1092, 1953.
- J. W. Milnor. *Morse Theory*. Number 51. Princeton University Press, 1963.
- K. Modin and G. Söderlind. Geometric integration of Hamiltonian systems perturbed by Rayleigh damping. *BIT Numerical Mathematics*, 51:977–1007, 2011.
- J. Møller, A. N. Pettitt, R. Reeves, and K. K. Berthelsen. An efficient Markov chain Monte Carlo method for distributions with intractable normalising constants. *Biometrika*, 93(2):451–458, 2006.
- M. Muehlebach and M. I. Jordan. Optimization with momentum: Dynamical, control-theoretic, and symplectic perspectives. *The Journal of Machine Learning Research*, 22(1):3407–3456, 2021.

- I. Murray, Z. Ghahramani, and D. MacKay. MCMC for doubly-intractable distributions. *arXiv preprint arXiv:1206.6848*, 2012.
- R. Neal. MCMC Using Hamiltonian Dynamics. In S. Brooks, A. Gelman, G. L. Jones, and X.-L. Meng, editors, *Handbook of Markov Chain Monte Carlo*, pages 113–162. Chapman & Hall/CRC, 2011.
- R. M. Neal. *Bayesian Learning for Neural Networks*, volume 118 of *Lecture Notes in Statistics*. Springer, New York, 1996. ISBN 978-0-387-94724-2.
- R. M. Neal. Slice sampling. *Annals of statistics*, pages 705–741, 2003.
- C. Nemeth, F. Lindsten, M. Filippone, and J. Hensman. Pseudo-extended Markov chain Monte Carlo. *Advances in Neural Information Processing Systems*, 32, 2019.
- Y. Nesterov. Primal-dual subgradient methods for convex problems. *Mathematical Programming*, (1): 221–259, 2009.
- L. I. Nicolaescu. *An Invitation to Morse Theory*. Springer, 2011.
- A. Nishimura and D. Dunson. Geometrically tempered Hamiltonian Monte Carlo. *arXiv preprint arXiv:1604.00872*, 2016.
- A. Nishimura, D. B. Dunson, and J. Lu. Discontinuous Hamiltonian Monte Carlo for discrete parameters and discontinuous likelihoods. *Biometrika*, 107(2):365–380, 2020.
- V. M. Panaretos and Y. Zemel. Statistical aspects of Wasserstein distances. *Annual review of statistics and its application*, 6:405–431, 2019.
- J. Park. Sampling from multimodal distributions using tempered Hamiltonian transitions, 2021.
- J. Park and M. Haran. Bayesian inference in the presence of intractable normalizing functions. *Journal of the American Statistical Association*, 113(523):1372–1390, 2018.
- B. T. Polyak and P. S. Shcherbakov. Optimisation and asymptotic stability. *International Journal of Control*, 91(11):2404–2410, 2018.
- E. Pompe, C. Holmes, and K. Łatuszyński. A framework for adaptive MCMC targeting multimodal distributions. *The Annals of Statistics*, 48(5):2930 – 2952, 2020.
- S. Reich. Backward error analysis for numerical integrators. *SIAM Journal on Numerical Analysis*, 36(5): 1549–1570, 1999.
- R. Rockafellar. *Convex Analysis*. Princeton Landmarks in Mathematics and Physics. Princeton University Press, 1997. ISBN 9780691015866.
- S. Sastry. *Nonlinear Systems: Analysis, Stability, and Control*, volume 10. Springer Science & Business Media, 2013.
- C. Sminchisescu and M. Welling. Generalized darting Monte Carlo. *Pattern Recognition*, 44(10):2738–2748, 2011.
- H. Strathmann, D. Sejdinovic, S. Livingstone, Z. Szabo, and A. Gretton. Gradient-free Hamiltonian Monte Carlo with efficient kernel exponential families. *Advances in Neural Information Processing Systems*, 28, 2015.

- H. Tak, X.-L. Meng, and D. A. van Dyk. A repelling-attracting metropolis algorithm for multimodality. *Journal of Computational and Graphical Statistics*, 27(3):479–490, 2018.
- M. A. Tanner and W. H. Wong. The calculation of posterior distributions by data augmentation. *Journal of the American Statistical Association*, 82(398):528–540, 1987. ISSN 01621459.
- L. Tierney. Markov chains for exploring posterior distributions. *the Annals of Statistics*, pages 1701–1728, 1994.
- N. Tripuraneni, M. Rowland, Z. Ghahramani, and R. Turner. Magnetic Hamiltonian Monte Carlo. In D. Precup and Y. W. teh, editors, *Proceedings of the 34th International Conference on Machine Learning*, volume 70 of *Proceedings of Machine Learning Research*, pages 3453–3461. Pmlr, 06–11 Aug 2017.
- D. A. van Dyk and X.-L. Meng. The art of data augmentation. *Journal of Computational and Graphical Statistics*, 10(1):1–50, 2001.
- A. Viorel, C. D. Alecsa, and T. O. Pința. Asymptotic analysis of a structure-preserving integrator for damped Hamiltonian systems. *Discrete and Continuous Dynamical Systems*, 41(7):3319–3341, 2020.
- Y. Zhang, Z. Ghahramani, A. J. Storkey, and C. Sutton. Continuous relaxations for discrete Hamiltonian Monte Carlo. *Advances in Neural Information Processing Systems*, 25, 2012.